Eur. Phys. J. A (2025) 61:89
https://doi.org/10.1140/epja/s10050-025-01551-3

THE EUROPEAN PHYSICAL JOURNAL A

Review

The α-nucleus potential: towards a solution of a long-standing problem

P. Mohr[1,a], Zs. Fülöp[1], Gy. Gyürky[1], Z. Halász[1], G. G. Kiss[1], S. R. Kovács[1,2], Zs. Mátyus[1,2], T. N. Szegedi[1], T. Szücs[1]

[1] HUN-REN Institute for Nuclear Research (ATOMKI), P.O.Box 51, Debrecen 4001, Hungary
[2] University of Debrecen, Doctoral School of Physics, Egyetem tér 1, Debrecen 4032, Hungary

Received: 26 February 2025 / Accepted: 21 March 2025

Communicated by David Blaschke

Abstract This study presents an overview over α-nucleus potentials which are the essential ingredient for the calculation of cross sections and astrophysical reaction rates for α-induced reactions on intermediate mass and heavy nuclei within the statistical model. Recent experimental data for Mo + α have been chosen as an example to illustrate the properties of several widely used α-nucleus potentials. The delicate role of the imaginary part of the potential at large radii is discussed which is the origin of the widely discrepant predictions of the different potentials at low energies far below the Coulomb barrier. The Atomki-V2 potential circumvents the complications with the imaginary part and provides very good predictions for the recent Mo + α data and also for most other recent reactions and is thus an excellent basis for the calculation of reaction rates. But further improvements are possible, and some ideas in this direction are given in the discussion.

1 Introduction

Reaction rates of α-induced nuclear reactions play a key role in many astrophysical scenarios. The ^{2}H(α,γ)^{6}Li and ^{3}H(α,γ)^{7}Li capture reactions are responsible for the lithium production in the big bang [1], and the ^{3}He(α,γ)^{7}Be reaction is essential for the understanding of the solar neutrino production in the pp-chain of hydrogen burning [2]. Helium burning is governed by the triple-α process via the Hoyle state [3,4], and the resulting carbon-oxygen ratio is defined by the ^{12}C(α,γ)^{16}O reaction [5]. The ^{18}Ne(α,p)^{21}Na reaction provides a route from hot CNO cycles to the NeNa and MgAl cycles and finally to the *rp*-process, and subsequent (α,p) reactions have major impact on the *rp*-process path [6,7]. The main neutron sources of the *s*-process are the ^{13}C(α,n)^{16}O and ^{22}Ne(α,n)^{25}Mg reactions [8,9]. A common property of all these reactions is that the astrophysical reaction rates are mostly governed by individual resonances and complemented by non-resonant contributions.

Contrary to the previous examples for light target nuclei with their small level densities, the reaction rates of α-induced reactions for heavy target nuclei result from the contributions of many overlapping resonances, corresponding to a high level density in the compound nucleus. Under these conditions, the appropriate theoretical approach is the statistical model [10]. The most important ingredient of the statistical model for α-induced reactions is the α-nucleus potential. It was found that the predictions of different potentials showed huge variations for the calculated reaction rates. It is the scope of this study to discuss the present status which has improved significantly in the last few years. The present study will not address the reactions for light targets which are mentioned in the first paragraph above. There are mainly two astrophysical processes where α-induced reaction rates for heavy targets are important.

First, the so-called weak *r*-process produces lighter heavy elements in the first *r*-process peak with $Z = 38 - 47$ under moderately neutron-rich conditions. The path of the weak *r*-process proceeds relatively close to the stability valley where β-decay half-lives are much longer than the timescale of the corresponding explosive events like core-collapse supernovae or neutron star mergers. Consequently, β-decay cannot drive the material towards higher charge numbers Z. As an alternative, (α,n) reactions have been identified, and a series of theoretical and experimental studies was published in the recent years (e.g., [11–14]).

Second, the nucleosynthesis of the neutron-deficient *p*-nuclei by a series of (γ,α), (γ,p), and (γ,n) reactions in the so-called γ-process [15–19] is strongly affected by α-nucleus

[a] e-mail: mohr@atomki.hu (corresponding author)

Published online: 28 April 2025

potentials. Typically, smaller uncertainties of about a factor of two are accepted for the (γ,p) and (γ,n) reaction rates, whereas much larger uncertainties for the (γ,α) reaction rates resulted from the choice of different α-nucleus potentials [20, 21]. The stellar (γ,α) reaction rates are related to the stellar (α,γ) reaction rates by detailed balance. It is much easier to constrain the stellar (α,γ) rate by experimental (α,γ) capture data than to constrain the stellar (γ,α) rate by experimental (γ,α) photodisintegration data, because thermal excitations of the target nuclei under stellar conditions are much more prominent in the (γ,α) channel than in the (α,γ) channel. Thus, the following discussion will focus on (α,γ) reactions although the astrophysically important quantity for the γ-process is the (γ,α) reaction rate.

The paper will be organized as follows. Sect. 2 will provide a brief introduction into the statistical model calculations which is complemented by some remarks on the typically underlying optical model and on the role of elastic scattering. Sect. 3 provides an overview over available α-nucleus potentials. Sect. 4 uses the example of ^{100}Mo + α to illustrate the achievements and limitations of the available α-nucleus potentials. The results will be discussed in Sect. 5, and finally conclusions are drawn in Sect. 6.

2 Theoretical approach

2.1 Statistical model

In a very schematic notation, the cross section $\sigma(\alpha,X)$ in the statistical model (SM) is given by

$$\sigma(\alpha, X) = \sigma_{\text{compound}} \times b_X \tag{1}$$

with the compound formation cross section σ_{compound} and the branching ratio b_X into the X channel. The compound formation and the decay are considered as independent in the first formulations of the SM [22,23]. Later, angular momentum conservation was included in the formalism [10], thus constraining the simplistic Eq. (1). Furthermore, correlations between the incident and outgoing waves are taken into account by a so-called width fluctuation correction factor (e.g., [24]) which is important mainly close to channel thresholds, but remains close to unity otherwise [25] except in a few exotic cases (e.g., [26]). The full formalism of the SM can be found e.g. in the review by Rauscher [25]. Despite its oversimplifcation, Eq. (1) nevertheless provides important insight because it allows a very descriptive interpretation; this will become obvious in the following discussion.

The branching b_X is given by

$$b_X = \frac{T_X}{\sum_i T_i} \tag{2}$$

with the transmissions T_i to the i-th decay channel. Each transmission T_i is composed of the sum over all final states j in the respective residual nucleus:

$$T_i = \sum T_{i,j} \tag{3}$$

In practice, the sum over the final states in Eq. (3) becomes very long, and thus the sum in Eq. (3) is splitted at a well-chosen j_{LD}, and all higher-lying levels are included by an integral over a theoretical level density (LD):

$$T_i = \sum_{j=0}^{j_{\text{LD}}} T_{i,j} + \int_{E^*(j_{\text{LD}})}^{E^*_{\text{max}}} \rho_{\text{LD}}(E^*)\, T_i(E)\, dE^* \tag{4}$$

Consequently, all T_i depend implicitly on the chosen LD in the respective residual nuclei. In practical calculations, often a relatively small $j_{\text{LD}} = 10$ is chosen; i.e., only the ground state and the lowest ten excited states are taken into account explicitly in the sum in the first term in Eq. (4) whereas all states above the excitation energy $E^*(10)$ of the 10$^{\text{th}}$ excited state are taken into account by the integral in the second term in Eq. (4).

The T_i are calculated within the optical model (OM) for the particle channels. As the most important channels are the proton, neutron, and α channel, global nucleon optical model potentials (NOMP) and global α-nucleus optical model potentials (AOMP) are required for these calculations. For the special case of the γ channel, the transmissions T_γ are derived from the γ-ray strength function (GSF).

The compound formation cross section σ_{compound} in Eq. (1) is usually taken as the total reaction cross section σ_{reac}. The latter can also calculated within the OM (although this is not a "must", and also other approaches could be used for the calculation of σ_{reac}; see Sect. 3.6). Within the OM, σ_{reac} scales with the transmission $T_{\alpha,0}$ in the entrance channel where the target nucleus is in its ground state in laboratory experiments. This leads to the following proportionality for the α-induced reaction cross section in the lab:

$$\sigma(\alpha, X) \sim T_{\alpha,0} \times \frac{T_X}{\sum_i T_i} \tag{5}$$

For the calculation of astrophysical reaction rates $N_A \langle \sigma v \rangle$, the entrance channel transmission $T_{\alpha,0}$ in Eq. (5) has to be extended to take into account thermal excitations of the target nucleus at the high temperatures of stellar conditions. This leads to the so-called stellar enhancement factor f_{SEF} (as e.g. defined in [27]). However, because of the Coulomb barrier, contributions of thermally excited states in the target nucleus remain relatively minor for (α,X) reactions, leading to enhancement factors f_{SEF} relatively close to unity for (α,X) reactions [27]. Contrary, huge f_{SEF} (up to factors of several thousand) are found for γ-induced reactions

[25,28]. A detailed analysis of laboratory cross sections and stellar reaction rates for the example of the ^{16}O(α,γ)^{20}Ne and ^{20}Ne(γ,α)^{16}O reactions is given in [29].

Because of the above mentioned definitions of the transmissions T_i into the different channels, in general the (α,X) cross section in Eq. (5) depends on all ingredients of the SM which are the NOMP, AOMP, GSF, and LD. However, a closer inspection of Eq. (5) shows that this equation can be simplified under certain circumstances, leading to (α,X) cross sections which depend essentially only on one or two ingredients of the SM. An experimental determination of the (α,X) cross sections for these special cases allows to constrain the parameters of the SM in a (more or less) unique way. Some examples will be listed below.

The first example is elastic (α,α) scattering. The analysis of angular distributions allows to derive information on the AOMP. But there are also ambiguities for the obtained parameters of the AOMP. A full discussion of elastic scattering and the resulting uncertainties for the derived parameters of the AOMP is beyond the scope of the present paper. For earlier work, see e.g. [30].

Another interesting information from the (α,α) angular distribution is the total reaction cross section $\sigma_{\rm reac}$. Its determination is less sensitive than the parameters of the AOMP and can be achieved down to energies significantly below the Coulomb barrier. Prerequisites for the determination of $\sigma_{\rm reac}$ are the measurement of the (α,α) angular distribution over the full angular range and a well-established deviation from the Rutherford cross section (e.g., by about 10 − 20% at backward angles, measured with small uncertainties below 5%). For a discussion of the resulting uncertainties of $\sigma_{\rm reac}$, see e.g. [31]. The available ^{100}Mo(α,α)^{100}Mo elastic scattering data will be discussed in Sect. 2.2.

In the further examples, the branching $b_X = T_X / \sum_i T_i$ in Eq. (5) comes close to unity, thus allowing to to constrain $T_{\alpha,0}$ and the underlying AOMP. In general, because of the missing Coulomb barrier, the transmission T_n to the neutron channel is dominating with $T_n \gg T_{i\neq n}$, leading to $\sum_i T_i \approx T_n$. At higher energies above the (α,2n) threshold, this changes to $\sum_i T_i \approx T_{1n} + T_{2n}$. Consequently, the ($\alpha$,$n$) cross section below the (α,2n) threshold depends only on $T_{\alpha,0}$ and thus only on the AOMP, but is almost independent of all the other ingredients of the SM like the NOMP, GSF, and LD. Above the (α,2n) threshold, the sum over the (α,1n) and (α,2n) cross sections depends only on the AOMP whereas the branching between the 1n and 2n channels is sensitive to the NOMP and LD of the residual nuclei. Interestingly, there are two different experimental techniques which have been used recently for the chosen example of ^{100}Mo + α: activation determines directly the (α,1n) cross section [32], and active-target experiments measure the total $Z \rightarrow Z + 2$ cross section which is essentially given by the sum over the (α,1n) and (α,2n) cross sections [33].

The last example with $b_X \approx 1$ is the (α,γ) cross section at low energies below the (α,n) threshold. For such low energies, the Coulomb barrier suppresses T_α whereas typical γ-ray transitions have strengths of the order eV or at least milli-eV. This leads to $T_\gamma \gg T_\alpha$ and $\sum_i T_i \approx T_\gamma$ because all other channels are closed. Consequently, the (α,γ) cross section below the (α,n) threshold depends only on $T_{\alpha,0}$ and thus only on the AOMP, but is – somewhat contra-intuitive – almost insensitive to the GSF.

Figure 1 shows the decomposition of the total reaction cross section $\sigma_{\rm reac}$ for ^{100}Mo + α into the different contributing (α,X) channels. The Atomki-V2 AOMP (see Sect. 3.6) was used for this calculation; the branchings b_X from other AOMPs will be not much different.

Figure 1 is composed of three parts. The upper part a) presents the cross sections $\sigma(E)$. Because of the Coulomb barrier, $\sigma(E)$ decreases dramatically towards low energies, leading to a variation of the total reaction cross section $\sigma_{\rm reac}$ by more than 10 orders of magnitude in the given energy range from 3 to 20 MeV. The same data are shown as astrophysical S-factor $S(E)$ in the middle part b). As usual for heavy nuclei, the total S-factor $S_{\rm reac}(E)$ decreases with energy because the transformation from cross section to S-factor overcompensates the energy dependence. It it obvious that the total cross section $\sigma_{\rm reac}$ (black dotted) is mainly composed of the (α,γ) cross section (red dashed) below the (α,n) threshold. Already a few hundred keV above the (α,n) threshold, the (α,n) channel dominates (blue full line), and about 1 − 2 MeV above the (α,2n) threshold the (α,2n) channel (brown long-dashed) becomes dominant. Other channels like the (α,p) channel (green dotted) and compound-elastic (light-blue dash-dotted) and compound-inelastic scattering (magenta dashed) remain below 5% at all energies under study. This becomes nicely visible in the lower part c) of Fig. 1 where the branching ratios b_X for the different channels are shown in a linear scale. As explained above, there are three different energy ranges: (i) Below the (α,n) threshold, the (α,γ) channel dominates with $b_\gamma \approx 1$. (ii) Above the (α,n) and below the (α,2n) threshold, the (α,n) channel dominates with $b_n \approx 1$. (iii) Above the (α,2n) threshold, the (α,1n) and (α,2n) channels contribute, leading to $b_{1n} + b_{2n} \approx 1$. Note that the ($\alpha$,3$n$) channel opens at 20.0 MeV, i.e. at the upper end of the energy range under study.

2.2 Elastic scattering

Elastic scattering plays an essential role for the prediction of (α,X) cross sections. The determination of all global AOMPs is finally based on the analysis of angular distributions of elastic scattering (see next Sect. 3). In practice, this is limited to energies above or around the Coulomb barrier. At energies far below the Coulomb barrier, the differential cross section approaches the Rutherford cross section for point-

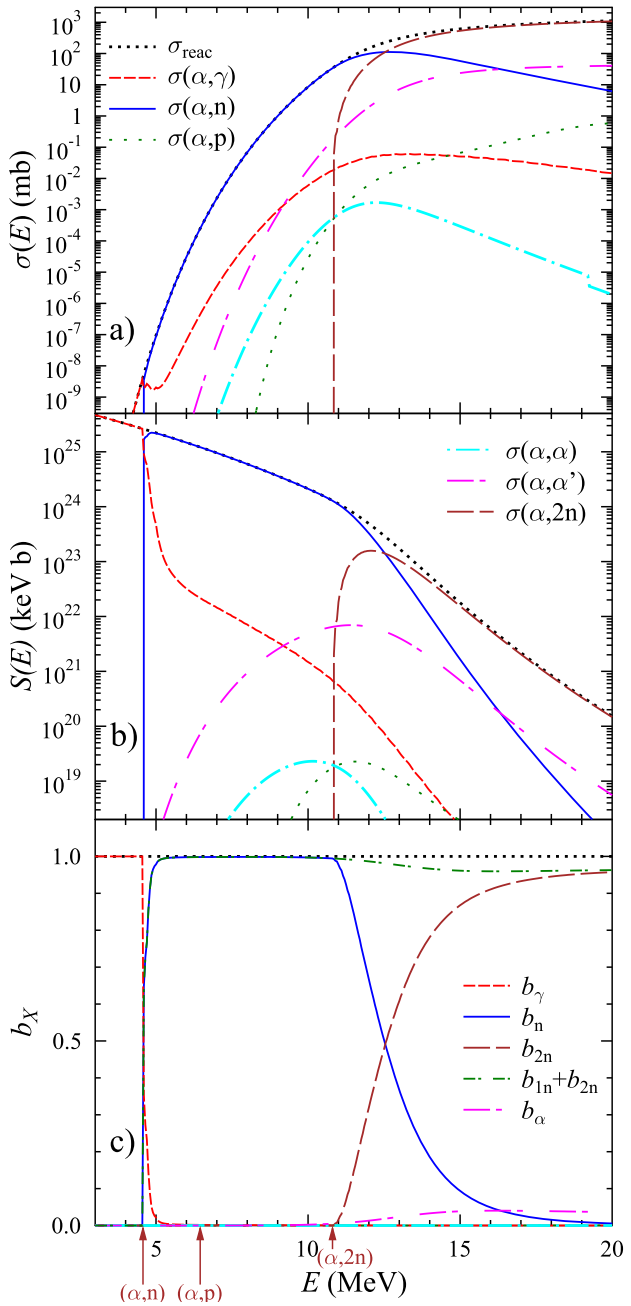

Fig. 1 Total reaction cross section σ_{reac} for ^{100}Mo + α and decomposition into the (α,X) channels: The upper part a) shows the cross section $\sigma(E)$; the middle part b) shows the same data as astrophysical S-factor. The lower part c) presents the branching ratios b_X from Eq. (2) in linear scale. The vertical arrows indicate the (α,n), $(\alpha,2n)$, and (α,p) thresholds. Further discussion see text

like charges; in such cases it becomes very difficult or even impossible to derive an AOMP from the experimental angular distribution. Even at energies around the Coulomb barrier, often ambiguities appear in the parameters of the AOMP (see e.g. [34]).

As already mentioned above, even in cases where it is difficult or impossible to determine the AOMP from the experimental angular distribution, elastic scattering can be used to determine the total reaction cross section σ_{reac} from the measured angular distribution. But unfortunately, the available ^{100}Mo$(\alpha,\alpha)^{100}$Mo elastic scattering data do not provide much information for the calculation of (α,X) reaction rates of ^{100}Mo + α because the scattering data do not reach low energies and do not cover the full angular range. The following analysis will show that a reliable local optimization of the AOMP for ^{100}Mo + α cannot be achieved from these scattering data. And also the determination of the total reaction cross section σ_{reac} is hampered by large uncertainties.

Three experimental angular distributions for ^{100}Mo$(\alpha,\alpha)^{100}$Mo elastic scattering are available at EXFOR [35,36]. The angular distribution by Matsuda et al. [37] at $E_{\alpha,\mathrm{lab}} = 30.82$ MeV covers an angular range from 17 to 72 degrees. Burger et al. [38] provide data in a similar range from 19 to 83 degrees at a slightly higher energy of 32.15 MeV. Note that the given energies $E_{\alpha,\mathrm{lab}}$ in both papers have been reduced by about 50 keV for the present analysis to take into account the energy loss in the relatively thick targets (about 1 mg/cm^2 in both works). Both data sets are listed in EXFOR without uncertainties, and it is stated that the data had to be digitized from the respective figures of the original works [37,38]. A re-analysis of these data suffers from limited precision of the re-digitization process and requires assumptions on the experimental uncertainties. As in both cases the final OM fitting parameters are given, we do not re-analyze these data here, but instead use the results from the original analysis. The angular distributions are shown together with the OM fits in Fig. 2.

OM potentials of Woods–Saxon (WS) type were used in [37] and [38]. (For a definition of the AOMP parameterizations, see Sect. 3.1.) Only one set of OM parameters is given in [37] for the data at 30.82 MeV. This leads to a total reaction cross section of σ_{reac} = 1572 mb. At 32.15 MeV three different fits are listed, leading to σ_{reac} between 1629 mb and 1869 mb. At first view, fit C (green dashed line) has a larger χ^2 and overestimates the data at larger scattering angles. However, fit C does a better job for the forward angles below 50°, and thus the lower σ_{reac} from fit C cannot be excluded. From the variations of σ_{reac}, an uncertainty about 150 mb can be estimated. Following the detailed investigation of uncertainties for σ_{reac} from elastic scattering in [31], this uncertainty of 150 mb from the WS analysis should still be considered as a lower limit of the real uncertainty because different parameterizations of the potential (like e.g. WS potentials or folding potentials) may lead to different σ_{reac}. Furthermore, the experimental data of [37,38] do not cover the full angular range.

The third angular distribution at $E_{\alpha,\mathrm{lab}} = 38.0$ MeV by Gontchar et al. is published in a journal which is not easily

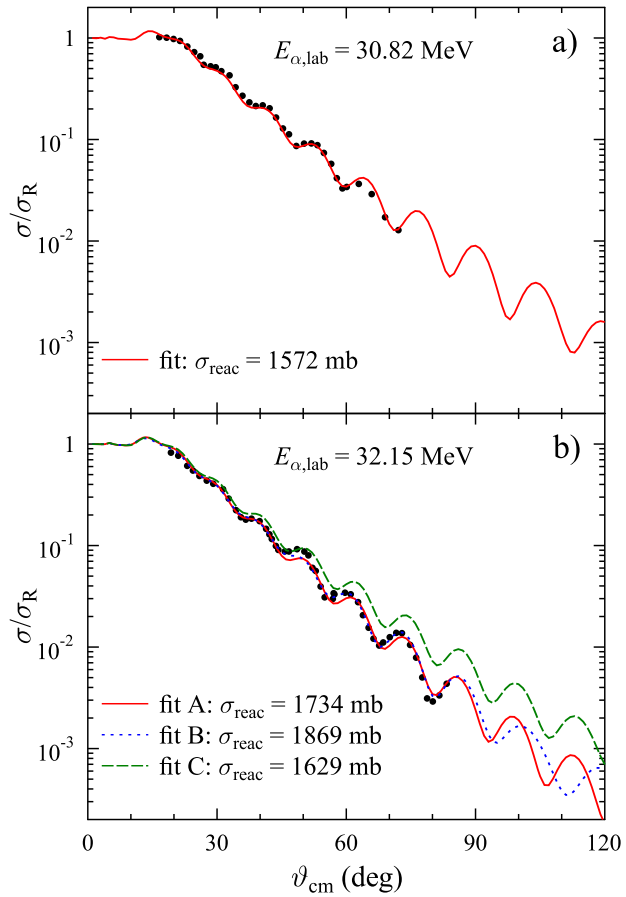

Fig. 2 Angular distributions of ^{100}Mo(α,α)^{100}Mo elastic scattering at $E_{\alpha,\mathrm{lab}}$ = 30.82 MeV (upper part a, [37]) and 32.15 MeV (lower part b, [38]), normalized to the Rutherford cross section. Fits from the original papers lead to the given total reaction cross sections σ_{reac}. Further discussion see text

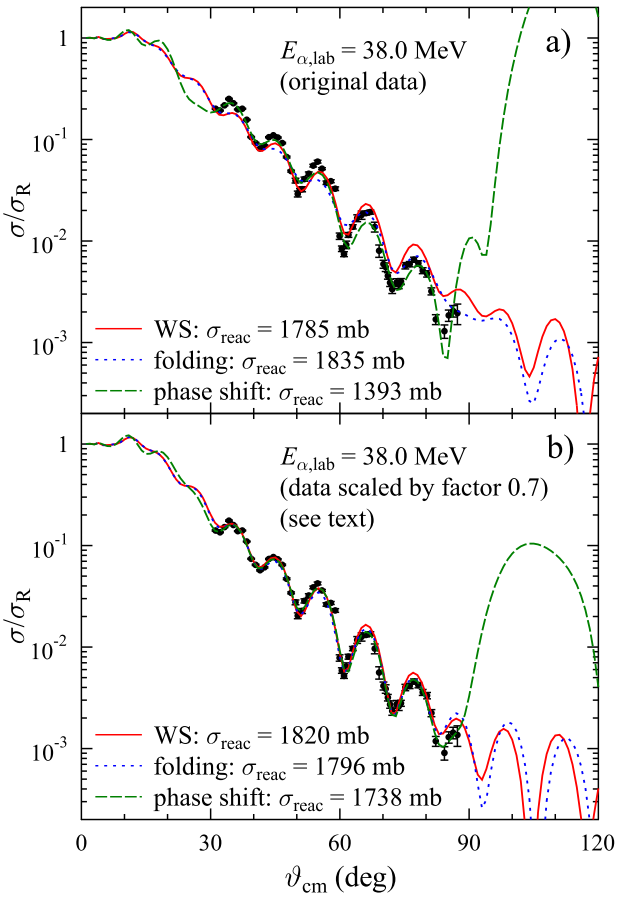

Fig. 3 Re-analysis of the angular distribution of ^{100}Mo(α,α)^{100}Mo elastic scattering at $E_{\alpha,\mathrm{lab}}$ = 38.0 MeV [39], using either the original data (upper part a) or data with an overall scaling factor of 0.7 (derived from the OM analysis, lower part b). Further discussion see text

accessible [39], but the data have been provided as numerical table to EXFOR (including the original experimental uncertainties). Thus, a re-analysis is feasible. The results can be found in Fig. 3.

Three fits were made for the angular distribution at 38 MeV. (*i*) Similar to the lower energies, potentials of volume WS type were used in the real and imaginary part of the AOMP. (*ii*) The real part of the AOMP was replaced by a folding potential (for details, see e.g. [30]). (*iii*) A model-independent phase shift analysis was made, using the approach of [40]. All fits are unable to reproduce the experimental data with $\chi^2/F \approx 1$, see Fig. 3, upper part a). At least the phase shift fit should achieve $\chi^2/F \approx 1$; otherwise, the experimental data cannot be described within the OM. Such a result points to problems with the experimental data. The 38 MeV data show tiny uncertainties of the order of 1% at the very forward angles, thus indicating that the given error bars are statistical uncertainties only. Systematic uncertainties are often not included in the angular distributions. Typically, systematic uncertainties are related to the target thickness, detector solid angle, and beam current integration. Often such uncertainties are of the order of 10 − 30% and affect all data points of the angular distribution in the same way.

So we have repeated the fits, using the experimental data with a free (fitted) absolute normalization, see Fig. 3, lower part b). In any case, normalization factors of about 0.7 are found. Furthermore, the fitted parameters behave more regularly; e.g., the width parameter w of the folding potential (see [30] and Sect. 3.1) remains very close to unity whereas a very unusual deviation from unity of 3% was found in the fit with fixed normalization. Also the phase shift fit is much closer to the AOMP fits at forward angles, and at angles beyond the experimental range the phase shift fit does not behave as strange as in the fit with fixed normalization. Furthermore, now the total cross sections σ_{reac} from the AOMP fits and the phase shift fit agree around 1800 mb whereas huge deviations between 1400 mb and 1800 mb were found for the fits with fixed normalization. Finally, we adopt σ_{reac}

$= 1785^{+50}_{-400}$ mb where the lower uncertainty results form the phase shift fit of the experimental data with fixed normalization.

It is interesting to see that the AOMP fits (using either WS or folding potentials) result in total cross sections of $\sigma_{\rm reac} \approx 1800$ mb, almost independent of the normalization of the experimental data. This can be explained by a geometric interpretation of the total reaction cross section. $\sigma_{\rm reac}$ is given by the integrated deviation between the Rutherford cross section (where $\sigma_{\rm reac} = 0$) and the experimental angular distribution; see e.g. Eqs. (4) and (5) in [31]. The Rutherford cross section decreases dramatically with increasing scattering angle $\sim \sin^{-4}(\vartheta/2)$. Consequently, the $\approx 90\%$ deviation from Rutherford ($\sigma/\sigma_R \approx 10^{-1}$) around $30° - 50°$ with $\sigma_R \approx 1500 - 200$ mb/sr contributes roughly similar to $\sigma_{\rm reac}$ as the $\approx 99\%$ deviation ($\sigma/\sigma_R \approx 10^{-2}$) around $60° - 80°$ with $\sigma_R \approx 110 - 40$ mb/sr. A careful look at the upper and lower parts of Fig. 3 shows that the AOMP fits can reproduce the experimental angular distribution around $\vartheta \approx 30° - 50°$ only for the scaled data in the lower part b) whereas the experimental data are clearly underestimated (and thus $\sigma_{\rm reac}$ is overestimated) for the original data in the upper part a). This means that the model space of the AOMP fits is too restricted to fit the original data, and any determination of total reaction cross sections $\sigma_{\rm reac}$ from such fits is somewhat questionable. Contrary to the AOMP fits, the phase shift fit is more flexible and provides a reasonable description of the experimental angular distribution at forward angles. These higher elastic cross sections in the phase shift fit lead to the low $\sigma_{\rm reac} = 1393$ mb.

The results for the total reaction cross sections from ^{100}Mo(α,α)^{100}Mo elastic scattering are summarized in Table 1. In addition so-called reduced energies $E_{\rm red}$ and reduced cross sections $\sigma_{\rm red}$ [41] are given which allow the comparison of various projectile-target combinations at different energies. The last column shows that the results are close to a reference calculation which is taken from ^{208}Pb + α in [31].

Unfortunately, the results for $\sigma_{\rm reac}$ in Table 1 cannot provide strong constraints for the AOMPs under study in the next Sect. 3 which predict $\sigma_{\rm reac}$ between 1409 and 1528 mb at 30.82 MeV, 1439 and 1612 mb at 32.15 MeV, and 1538 and 1744 mb at 38.0 MeV. All predictions are somewhat lower than the experimental values, but roughly within the experimental error bars (which may still be optimistic; see above discussion). This is a general result that various AOMPs lead to similar total reaction cross sections $\sigma_{\rm reac}$ at energies above the Coulomb barrier. Major differences in the predictions are only found for low energies far below the Coulomb barrier which is the most relevant energy range for the calculation of astrophysical reaction rates $N_A \langle \sigma v \rangle$. This will be explained below.

The findings from the analysis of the elastic scattering angular distributions can be summarized as follows. First, it is difficult to determine the total reaction cross section $\sigma_{\rm reac}$ from the available ^{100}Mo(α,α)^{100}Mo angular distributions with small uncertainties. This is related to the limited data quality (limited angular range and uncertain absolute normalization) and also related to restrictions of the model space in AOMP fits. Second, $\sigma_{\rm reac}$ from elastic scattering at energies above the Coulomb barrier are reasonably well predicted by all recent AOMPs, and thus no strong conclusion on the AOMPs can be derived from the available elastic scattering data. The latter conclusion might change if angular distributions of excellent quality become available at energies around the Coulomb barrier.

3 Available α-nucleus potentials

3.1 Definitions

The total reaction cross section $\sigma_{\rm reac}$ in the OM is related to elastic scattering by the well-known formula

$$\sigma_{\rm reac} = \frac{\pi}{k^2} \sum_L (2L+1)\,(1 - \eta_L^2) \tag{6}$$

where $k = \sqrt{2\mu E}/\hbar$ is the wave number, E is the energy in the center-of-mass (c.m.) system, and η_L are the real reflexion coefficients. The reflexion coefficients η_L and the phase shifts δ_L are calculated by solving the Schrödinger equation for a complex OM potential. It is important to note that the imaginary part of the potential is essential for the damping of the outgoing wave function, leading to $\eta_L < 1$ and thus a finite total reaction cross section $\sigma_{\rm reac}$ in Eq. (6). A potential without imaginary part in the OM leads to $\eta_L = 1$ for all partial waves and thus a vanishing $\sigma_{\rm reac} = 0$ in Eq. (6). The interplay of the real and imaginary parts of the potential will be discussed later in more detail (see Sect. 3.3).

The complex OM potential for the interaction of charged particles is given by

$$U_{\rm OM}(r) = V(r) + iW(r) + V_C(r) \tag{7}$$

where $V(r)$, $W(r)$, and $V_C(r)$ are the real part, imaginary part, and Coulomb part of the OM potential $U_{\rm OM}(r)$. Typical parameterizations for the potentials $V(r)$, $W(r)$, and $V_C(r)$ are listed in the following.

The Coulomb potential $V_C(r)$ is often used in the simple form of a homogeneously charged sphere with the radius parameter $R_C = R_{C,0} \times A_T^{1/3}$ in the light-ion convention; A_T is the mass number of the target nucleus. Typically, the calculations are not very sensitive to the choice of the Coulomb radius R_C, and in many cases either $R_{C,0} = 1.3$ fm is used, or R_C is taken identical as the root-mean-square radius of

Table 1 Total reaction cross sections σ_{reac} and reduced energies E_{red} and reduced cross sections σ_{red} from the analysis of ^{100}Mo(α,α)^{100}Mo elastic scattering. The last column shows the ratio to a reference calculation for ^{208}Pb + α in [31]

$E_{\alpha,lab}$ (MeV)	σ_{reac} (mb)	E_{red} (MeV)	σ_{red} (mb)	$\sigma_{red}/\sigma_{red}(\alpha)$
30.82	1572 ± 150	2.20	40.5	1.21
32.15	1744 ± 150	2.29	44.9	1.32
38.0	1785^{+50}_{-400}	2.71	46.0	1.25

the nuclear potential $V(r)$. In some works V_C was also calculated by a folding procedure with the Coulomb interaction; see also Eq. (11) below.

The real and imaginary parts of the OM are widely parametrized by the Woods-Saxon shape; e.g., for the real part this reads

$$V(r) = -V_0 \times f_{WS}(x) \tag{8}$$

with the potential depth V_0 and the WS function

$$f_{WS}(x) = \frac{1}{1 + \exp(x)} \tag{9}$$

with $x = (r - R_V)/a_V$, the radius parameter $R_V = R_{V,0} \times A_T^{1/3}$, and the diffuseness a_V. A similar definition is used for the imaginary part of volume type with the parameters W_V, R_W, and a_W. In addition, often a surface-type imaginary potential is added

$$W(r) = W_S \times \frac{df_{WS}(x)}{dx} \tag{10}$$

with the parameters W_S, R_S, and a_S. Note that maximum depth of the imaginary surface potential $W(r)$ at $r = R_S$ is $W_{max}(r) = -W_S/4$ in the definition of Eq. (10). Also square and cubic forms of Eq. (9) and further modifications have been used in literature.

A more microscopic approach for the real part of the OMP is obtained from the folding procedure

$$V_F(r) = \int\int \rho_P(r_P)\, \rho_T(r_T)\, v_{eff}(s)\, d^3r_P\, d^3r_T \tag{11}$$

with the nucleon densities $\rho_{P,T}(r_{P,T})$ of projectile and target and an effective energy- and density-dependent nucleon-nucleon (NN) interaction $v_{eff}(s)$. Finetuning of the folding potential, e.g. for fitting of angular distributions of elastic scattering, is achieved by the introduction of two parameters λ and w, leading to

$$V(r) = \lambda\, V_F(r/w). \tag{12}$$

λ is the strength parameter of the order of $\lambda \approx 1.1 - -1.4$ leading to real volume integrals[1] of about $J_R \approx 350$ MeV fm^3 [30,42]. $w \approx 1$ is the width parameter which should remain very close to unity within about $1 - 2\,\%$; a larger deviation of w from unity would indicate a failure of the underlying folding model.

The above formalism assumes spherical symmetry of the AOMPs and neglects deformation. It must be pointed out that the parameters of the various AOMPs under discussion (see below) have been adjusted to experimental data with this assumption of spherical symmetry. Thus, deformation is implicitly included in the obtained parameters of the AOMPs. If deformation were added to these potentials, then the relevance of deformation would be double-counted. For a consistent treatment of deformation, a new deformed global AOMP has to be determined by re-fitting the experimental data in a non-spherical approach.

3.2 General remarks

Several AOMPs are available in literature. The present investigation will focus on selected AOMPs which are implemented in the widely used computer code TALYS [43,44] in the versions V1.80 and V1.96. In particular, the behavior at low energies has to be studied for a reliable prediction of astrophysical reaction rates. Here some general properties of AOMPs will be identified which allows to estimate also the applicability of other AOMPs for the calculation of low-energy cross sections and astrophysical reaction rates. An overview of the AOMPs under detailed study is listed in Table 2.

Three more AOMPs are implemented in TALYS. Option "*alphaomp* 1" corresponds to a simplified folding approach which is based on the analysis of high-energy deuteron scattering by Watanabe [50] in 1958. "*alphaomp* 7" is taken from Nolte et al. [51] where elastic α scattering was investigated at energies above 80 MeV and up to 172 MeV. "*alphaomp* 8" was derived as an extension of the Nolte et al. AOMP from a series of (n,α) data around target masses of $A \approx 50$ by Avrigeanu et al. [52]. As these AOMPs have been derived from scattering data at much higher energies, it is not very surprising that the resulting predictions of low-energy reac-

[1] As usual, the negative signs of the volume integrals J_R and J_I are omitted in the discussion.

Table 2 Overwiew of the AOMPs under detailed study in the present investigation: McFadden/Satchler-1966 (MCF), Demetriou-2002 (DEM) in three versions, Avrigeanu-2014 (AVR), and Atomki-V2-2020 with the corresponding TALYS parameter *alphaomp*, Woods-Saxon (WS) or folding (fold) parameterization (par.), and energy dependence (ED)

Abbrev.	TALYS	Ref.	Real part		Imag. part	
	alphaomp		Par.	ED	Par.	ED
MCF	2	[45]	WS	N	WS	N
DEM-1	3	[46]	fold	Y	WS	Y
DEM-2	4	[46]	fold	Y	WS	Y
DEM-3	5	[46]	fold	Y	WS	Y
AVR	6[1]	[47]	WS	Y	WS	Y
Atomki-V2	9[2]	[48]	fold	N	WS	N

[1]TALYS default option
[2]modified versions of TALYS-V1.80 and TALYS-V1.96; see explanation in [49]

tion cross sections are inferior to the AOMPs in Table 2. No further discussion of these high-energy AOMPs is provided in the present study.

In the following, the AOMPs in Table 2 are presented in greater detail in Sects. 3.3, 3.4, 3.5, and 3.6. There are further recent AOMPs which are not yet implemented into TALYS, and thus these AOMPs cannot be used in a simple way. Nevertheless, as already pointed out above, there are general properties of the AOMPs under study which allow to assess also other recent AOMPs. This information is provided in Sect. 3.7.

Before we start with the discussion of the various AOMPs, we list the energies of the Gamow window which defines the astrophysically most relevant energies. For the chosen example of ^{100}Mo + α, the energies of the classical Gamow windows for temperatures between $T_9 = 1-5$ are listed in Table 3. (As usual, T_9 is the temperature in Giga-Kelvin.) For completeness it must be noted that the real Gamow windows are slightly shifted towards lower energies because of the negative slope of the astrophysical S-factor (for details, see [53]). The Gamow window may be further affected for (α,n) reactions with negative Q-values which is $Q = -4572$ keV in the case of the ^{100}Mo(α,n)^{103}Ru reaction. This restriction is mainly relevant for stable target nuclei whereas for neutron-rich nuclei in the weak r-process the Q-values of the (α,n) reaction become close to zero or even positive.

3.3 McFadden and Satchler (1966)

The widely used AOMP by McFadden and Satchler (MCF) [45] was derived in the 1960s from elastic scattering data for target nuclei between ^{16}O and ^{238}U at 24.7 MeV. WS potentials of volume type were used throughout that study; i.e., six parameters (depth, radius, and diffuseness of the real and imaginary part of the AOMP) were adjusted to the experimental angular distributions. It was found that there are many ambiguities in the parameters of the AOMP, and local 4-parameter fits (using the constraints $R_V = R_W$ and $a_V = a_W$), 5-parameter fits (using the constraint $R_V = R_W$), and 6-parameter fits are presented. At the end, it is concluded that the 5-parameter fits and 6-parameter fits do not lead to significant improvement in the description of the angular distributions, and a global 4-parameter fit is given as the final result: $V_0 = -185$ MeV, $W_0 = -25$ MeV, $R_{V,0} = R_{W,0} = 1.4$ fm, $a_V = a_W = 0.52$ fm.

This simple 4-parameter AOMP was later used as the so-called McFadden/Satchler AOMP in many subsequent studies, including the calculations with the statistical model code NON-SMOKER [55] which were adopted in the REACLIB database [56]. As the MCF AOMP was determined from elastic scattering data at only one energy of 24.7 MeV, no energy dependence was given, and consequently, the parameters of the MCF AOMP were taken as energy-independent in all subsequent studies.

Whereas the extremely simple MCF AOMP provides very reasonable predictions for the total reaction cross section σ_{reac} at energies above the Coulomb barrier (see also Sect. 2.2 above), data far below the Coulomb barrier are dramatically overestimated. This became first obvious in the analysis of the pioneering experiment for the ^{144}Sm(α,γ)^{148}Gd reaction by Somorjai et al. [57]. It was found in this work that an additional energy dependence of the depth of the imaginary part with a so-called Fermi function leads to a much better description of the experimental (α,γ) data:

$$W_V(E) = \frac{W_{V,0}}{1 + \exp\left[(E_F - E)/a_E\right]} \tag{13}$$

Here $W_{V,0} = 25$ MeV is the depth of the original MCF AOMP, and the parameters E_F and a_E were adjusted to the (α,γ) data. A similar parameterization of the energy dependence was later used in several subsequent studies, see e.g. [58–65]. Often, E_F in Eq. (13) is fixed to $E_F = 0.9\,E_C$ where E_C is the height of the Coulomb barrier; this energy E_F is

Table 3 Classical Gamow window (center energy E_0 and width Δ) for ^{100}Mo + α. $E_{0,\mathrm{red}}$ is the reduced Gamow energy (as defined in [41]; see also Sect. 2.2). Properties of $E_{0,\mathrm{red}}$ are discussed in [54]

T_9	kT (keV)	E_0 (keV)	Δ (keV)	$E_{0,\mathrm{red}}$ (keV)
1	86	3666	1298	272
2	172	5820	2314	432
3	259	7626	3243	566
4	345	9238	4122	685
5	431	10720	4965	795

also called E_2 and parametrized in [66]. The obtained parameter a_E varies between about 2 MeV and 10 MeV, where a smaller a_E reduces the predicted sub-Coulomb cross sections stronger than a larger a_E. The impact of a_E at higher energies remains relatively minor.

The failure of the MCF AOMP at sub-Coulomb energies and the uncertain energy dependence of the imaginary part from the different a_E has motivated us to investigate the role of the imaginary part of the AOMP in further detail. At energies above the Coulomb barrier, the total reaction cross section σ_{reac} in Eq. (6) saturates around 1800 mb for the chosen example of ^{100}Mo + α (see Sect. 2.2). This corresponds to absorption of a black disk with a radius R_{disc} which is related to $\sigma_{\mathrm{reac}} = \pi R_{\mathrm{disc}}^2$; i.e., $R_{\mathrm{disc}} \approx 7.5$ fm. As expected, this R_{disc} roughly corresponds to the sum of the radii of the colliding ^{100}Mo and ^{4}He nuclei. Each AOMP with a reasonable range is able to reproduce such σ_{reac} above the Coulomb barrier. This is in line with the findings in Sect. 2.2 that all AOMPs under study describe the σ_{reac} between 30 MeV and 40 MeV.

At lower energies slightly below the barrier, the calculated σ_{reac} results from the interplay of (*i*) the tunneling probability of the incoming α particle through the barrier in the real part of the AOMP and (*ii*) the absorption by the imaginary part of the AOMP in the interior after tunneling. Here σ_{reac} becomes sensitive to the real part and to the imaginary part of the AOMP. But still here the differences between various AOMPs are not too dramatic as long as the AOMPs are well constrained from elastic scattering.

However, at extremely low energies far below the Coulomb barrier, the sensitivity of the calculated σ_{reac} changes dramatically [67]. The transmission probability through the Coulomb barrier becomes so small that the damping of the wave function by the imaginary part occurs mainly at large radii far outside the colliding nuclei, but not in the nuclear interior (i.e., absorption occurs without tunneling). As a consequence, the calculated σ_{reac} is sensitive mainly to the tail of the imaginary part at large radii, but almost insensitive to the interior of the imaginary part and also almost insensitive to the real part of the AOMP. These findings are illustrated in Figs. 4 and 5.

Figure 4 shows the ratios of the total reaction cross section $\sigma_{\mathrm{reac}}/\sigma_{\mathrm{reac}}$(MCF) for different modifications of the imaginary part of the MCF potential where σ_{reac}(MCF) is the cross section which is calculated from the standard MCF potential (as described above). The shown energy range between 3 MeV and 20 MeV covers 17 orders of magnitude for σ_{reac}(MCF) from about 10^{-17} b at the lowest energy up to about 1 b at the highest energy.

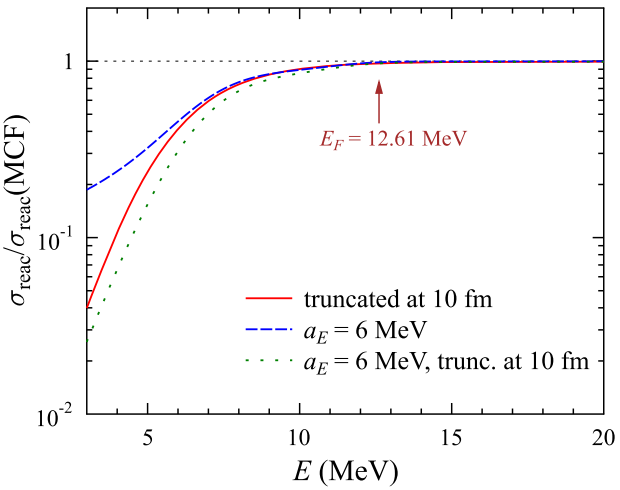

Fig. 4 Ratio $\sigma_{\mathrm{reac}}/\sigma_{\mathrm{reac}}$(MCF) for different modifications of the imaginary part of the MCF potential: truncated at $r = 10$ fm (full red line), energy-dependent according to Eq. (13) with $a_E = 6$ MeV (blue dashed), and energy-dependent and truncated at 10 fm (green dotted). The vertical arrow indicates the energy $E_F = 0.9\, E_C = 12.61$ MeV in Eq. (13) for ^{100}Mo + α where the imaginary strength is reduced by a factor of two. Further discussion see text

As first modification, a truncation of the imaginary potential at $r = 10$ fm (full red line in Fig. 4) is applied. This has only minor impact at energies above the Coulomb barrier. Contrary, the calculated σ_{reac} becomes much lower towards lower energies. E.g., at 5 MeV σ_{reac} drops by a factor of about 4.2, whereas at 15 MeV the reduction of σ_{reac} remains tiny with about 1%. Below about 4 MeV, less than 10% of σ_{reac} result from the nuclear interior ($r \leq 10$ fm).

The corresponding imaginary part of the potential is shown in Fig. 5 (long-dashed black line for the original MCF AOMP, full red line for the truncated imaginary part). Note that the depth of the imaginary part is only about 30 keV at the truncation at $r = 10$ fm, i.e., around 0.1% of the central depth of $W_V = 25$ MeV. This means that the tiny tail of the imaginary part of the potential at large radii above 10 fm is responsible for the dominating contribution of σ_{reac} at the astrophysically relevant energies in the Gamow window.

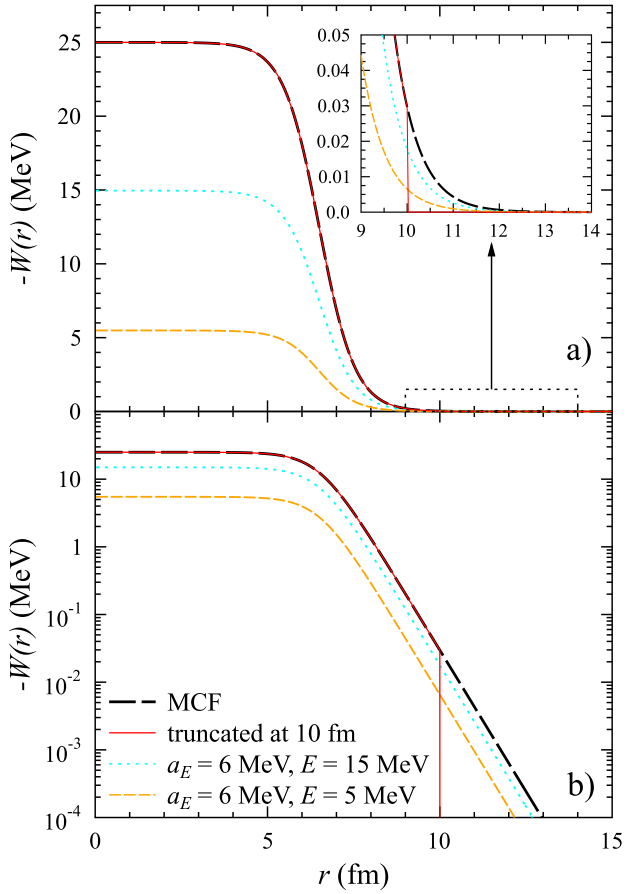

Fig. 5 Imaginary part of the MCF AOMP and different modifications: original MCF (long-dashed black line), truncated at $r = 10$ fm (full red), and energy-dependent with $a_E = 6$ MeV at $E = 15$ MeV (light-blue dotted) and at $E = 5$ MeV (orange dashed). The upper part a) shows a linear scale and an inset for the tail of the imaginary part at large radii; the lower part b) shows the same data in a logarithmic scale. Further discussion see text

Interestingly, a very similar result for $\sigma_{\rm reac}$ is obtained when the truncation of the imaginary part at $r = 10$ fm is replaced by the second modification which is an energy dependence according to Eq. (13). Figure 4 shows the result using $a_E = 6$ MeV (blue dashed) which is in the center of suggested a_E from previous work [58–65]. At $E = E_F = 12.61$ MeV $\sigma_{\rm reac}$ is reduced by only 1.5% although the overall strength of the imaginary potential is reduced by a factor of two at E_F. Even smaller changes are found for higher energies above E_F. A further truncation at $r = 10$ fm of the energy-dependent imaginary part with $a_E = 6$ MeV has relatively minor impact above 8 MeV, but reduces $\sigma_{\rm reac}$ further towards very low energies. Two examples for the imaginary potential with $a_E = 6$ MeV are shown in Fig. 5 for $E = 5$ MeV (orange dashed line) and 15 MeV (lightblue dotted).

Summarizing this discussion, we find that the total reaction cross section $\sigma_{\rm reac}$ at astrophysically relevant energies is mainly sensitive to the tail of the imaginary potential at larger radii beyond $r = 10$ fm. Using the original MCF AOMP, this leads to a dramatic overestimation of $\sigma_{\rm reac}$ at low energies. This overestimation can be compensated either by truncating the imaginary part of the AOMP at $r = 10$ fm or by introducing an energy dependence of the imaginary potential according to Eq. (13). As this tail of the imaginary potential (with typical tiny strengths of 0.1% of the central depth) is not at all constrained in the construction of an AOMP from the fitting of elastic scattering, it seems to be more natural to use the first approach and truncate the imaginary potential at large radii. This is also consistent with a naive view on the formation of a compound nucleus which does not occur outside the colliding nuclei. Furthermore, this truncation avoids numerical complications. Without truncation, the calculated $\sigma_{\rm reac}$ becomes sensitive to the chosen maximum radius $R_{\rm max}$ in the integration of the Schrödinger equation. (Such a sensitivity may even remain completely unnoticed as long as one uses the TALYS code which sets a well-chosen pre-defined $R_{\rm max}$ automatically.) This idea of truncation of the imaginary part will be followed later in the construction of the Atomki-V2 AOMP (see Sect. 3.6).

3.4 Demetriou et al. (2002)

Demetriou et al. [46] (DEM) provide three versions of a global AOMP which is based on a folding potential in the real part and a WS potential in the imaginary part. The folding potential in the real part applies the so-called DDM3Y nucleon-nucleon interaction [68,69] which leads to an intrinsic energy dependence of the folding potential from the chosen interaction. In addition, an explicit energy dependence for the volume integral J_R is taken from the parameterization of [70] with refitted parameters. The imaginary part in the first version (DEM-1) of the DEM AOMPs is taken as a volume Woods-Saxon; a surface term is added in the second version (DEM-2). The third version (DEM-3) uses a volume WS plus a damped surface WS in the imaginary part; in addition a dispersive coupling between the real and imaginary parts of the AOMP is applied.

The parameters of the DEM potentials were adjusted to fit experimental data which were available more than 20 years ago. The experimental data consisted of low-energy elastic scattering for targets between ^{40}Ca and ^{208}Pb and of a series of (α,n), (α,p), (α,γ), and (n,α) reaction data. Only very few low-energy reaction data were available for target nuclei with masses above $A \approx 100$, including the Somorjai et al. data for ^{144}Sm$(\alpha,\gamma)^{148}$Gd from 1998 [57]. In a later experiment by Scholz et al. [71], the data by Somorjai et al. were essentially confirmed, but there is some tension between both experiments for the data points at their lowest energies. Whereas Scholz et al. give an S-factor (all S-factors in 10^{26} MeV b) of 11.6 ± 0.8 at $E = 10.675$ MeV, the result by Somorjai et al. of 7.13 ± 2.92 at $E = 10.193$ MeV is roughly a factor of

1.6 lower. Furthermore, a minor correction to the Somorjai et al. activation data was applied in [71] to take into account a more accurate half-life of the residual ^{148}Gd nucleus, leading to an even lower result of 6.8 ± 2.8.

Because of the huge deviation between the experimental ^{144}Sm(α,γ)^{148}Gd data by Somorjai et al. and the calculation with the MCF AOMP, much efforts have been spent in the following years to fit the energy dependence of the Somorjai et al. data, including the lowest data point with its very low S-factor with 40% uncertainty. The consequence was a strong energy dependence of the fitted AOMP to fit the low S-factor at the lowest energy. Nowadays, combining the lowest data points of Somorjai et al. and Scholz et al. leads to a somewhat different behavior of the low-energy S-factor of the ^{144}Sm(α,γ)^{148}Gd reaction which would also weaken the derived energy dependence of the AOMP. Because the ^{144}Sm(α,γ)^{148}Gd data by Somorjai et al. are the only fitted (α,γ) data above $A = 100$ in the DEM study, it is not surprising that the DEM AOMPs (in all versions) have a trend to underestimate reaction cross sections at sub-Coulomb energies.

For completeness we note that a small modification to the DEM AOMPs was implemented in the recent TALYS−1.96 version which is not well-documented. The modification claims to achieve better agreement with experimental data by taking into account deformation. This is achieved by an adjustment of the radius R_W of the imaginary potential which increases slightly with positive deformation parameter β_2. Such an increased imaginary radius leads to increased low-energy cross sections, thus probably compensating the fact that the original DEM AOMPs tried to fit the low S-factor of the Somorjai et al. data. As pointed out above, such an addition of deformation (without refitting the whole AOMP) may lead to double-counting the relevance of deformation. Furthermore, for nuclei with $\beta_2 < 0$ (as e.g. for the case of ^{120}Te), the modification leads to smaller cross sections from the DEM AOMPs; here the deviations to the latest experimental data are increased by the modification [72].

3.5 Avrigeanu et al. (2014)

The AOMP by Avrigeanu et al. [47] (AVR) follows a very similar approach as the previous DEM AOMPs. The basis of this AVR AOMP is a double-folding potential in the real part in combination with a WS imaginary part where the parameters were first adjusted to elastic scattering data [73]. Later, the study was extended to (α,X) and (n,α) reactions in [74], and the double-folding potential in the real part was replaced by a so-called "DF-equivalent Woods-Saxon potential". A careful fine-tuning of the WS parameters was performed to fit the available (α,X) and (n,α) data. Finally a many-parameter AOMP is obtained [66]. Further improvement was achieved by an additional investigation of the level density [47]. This study [47] from 2014 was implemented in TALYS. Later tests in a series of subsequent papers (e.g. in [75–77]) essentially confirmed the obtained parameters with minor modifications.

It is interesting to note that already in the study from 2010 [66] it was noticed that "The energy dependence of the surface imaginary potential depth is proved to be essential for the understanding of the α-particle interaction behavior below the Coulomb barrier". However, the essential role of the tail of the imaginary potential at large radii was not noticed at that time.

Compared to the previous DEM AOMPs from 2002, the AVR AOMP could be adjusted to a much larger database for (α,γ) and (α,n) reaction data at low energies which became available in the meantime. Consequently, the AVR AOMP provides a better descrioption of the low-energy data for many cases. However, it was noticed recently in the analysis of (α,n) data for tellurium isotopes $^{120\text{-}130}$Te that the AVR AOMP systematically underestimates the latest experimental data. This is probably related to the fact that the only one data set for ^{120}Te(α,n)^{123}Xe at that time by Palumbo et al. [78] was used for adjustment in [47]. These data of [78] consist of three data points only which are lower than the latest data by Mátyus et al. [72].

Summarizing, the many-parameter AVR AOMP is able to reproduce a lot of (α,α), (α,n), (α,γ), and (n,α) data for a wide range of target nuclei with very good accuracy. However, the determination of the many energy-dependent parameters of the AVR AOMP requires the availability of excellent reaction data in a wide range of target nuclei and in a wide range of energies, as close as possible to the astrophysically most relevant Gamow window. Furthermore, under these conditions the extrapolation to unstable nuclei must remain somewhat uncertain.

3.6 Atomki-V2 (2020)

Contrary to the above DEM and AVR AOMPs, the Atomki-V2 AOMP [48,49] is based on a completely different approach which avoids the complications which result from the importance of the tail of the imaginary part (as shown above in Fig. 4 for the MCF AOMP). The compound formation cross section $\sigma_{\text{compound}} \approx \sigma_{\text{reac}}$ in Eq. (1) is derived from a simple barrier transmission calculation which is also widely used in heavy-ion fusion [79–81]; i.e., σ_{reac} is calculated from the transmission in a purely real potential, thus avoiding any dependence on the imaginary part which is not required in the barrier transmission model.

Of course, the real part of the potential needs to be well constrained in this approach. In previous work, from a series of elastic scattering experiments at energies around the Coulomb barrier in our institute, we have derived an AOMP called "Atomki-V1" which turns out to be very appropriate here [30]. The real part of Atomki-V1 is based on the fold-

ing approach (very close to the DEM AOMP). It is energy-independent and shows also only a small dependence on the target nucleus with a slightly reduced strength parameter λ in Eq. (11) and volume integral J_R for magic and semi-magic target nuclei. It is shown in [48] that this approach leads to an excellent reproduction of the available experimental data for heavy nuclei. This will be discussed in further detail below in Sect. 5.

The barrier transmission approach allows to calculate the total reaction cross section σ_{reac}, but not the various (α,γ), (α,n), or (α,p) cross sections. The calculation of the individual exit channels requires to use the statistical model and a corresponding computer code. So we have decided to complement the real part of the Atomki-V1 potential with a deep, narrow, and sharp-edged imaginary WS potential with $W_V = 50$ MeV, $R_{W,0} = 1.0$ fm, and $a_W = 0.1$ fm. This AOMP has been added to a modified version of TALYS.

The combination of the real part of Atomki-V1 and the sharp-edged imaginary WS potential is called Atomki-V2. The above construction ensures that the total cross section σ_{reac} in the OM calculation is almost identical to the fusion cross section in the barrier transmission approach. This can be explained by the following considerations. The fusion cross section in the barrier transmission approach results from the tunneling through the barrier. In the OM, the incoming α has to tunnel through the barrier in a similar way as in the transmission approach. As soon as the incoming α has succeeded to tunnel through the barrier, it is absorbed by the imaginary potential in the interior. The above choice of a deep, narrow, and sharp-edged imaginary part ensures that the transmission and absorption in the OM are practically decoupled, and that all incoming α particles are indeed absorbed (if the imaginary part has a sufficient depth). No absorption occurs outside the barrier because of the chosen geometry of the imaginary part (small radius and very small diffuseness). For further discussion of the relation between the barrier transmission approach and the OM approach with a deep, narrow, and sharp-edged imaginary potential, see also [82,83].

The Atomki-V2 AOMP is completely determined by elastic scattering data at energies around the Coulomb barrier [30]. Thus, it allows to predict the total reaction cross section σ_{reac} without any adjustment to (α,X) reaction data; there are no adjustable parameters for Atomki-V2. Thus, any uncertainties from purely constrained fitting parameters or any sensitivity on the quality and availability of experimental (α,X) data are completely avoided, leading to reliable and robust predictions for a wide range of target nuclei. Overall, predictions from the Atomki-V2 AOMP typically deviate from experiment by far less than a factor of two (with one noticable exception of ^{88}Sr [84]; see Sect. 5).

3.7 Other recent AOMPs

As already mentioned above, the present study focuses on those AOMPs which are available in the TALYS code (or have been implemented by ourselves in the case of the Atomki-V2 AOMP). Such an implementation for AOMPs from literature requires at least some efforts, and in many cases it is not even possible because the published information is not sufficient to re-calculate the real and imaginary parts of those AOMPs. The latter statement holds in particular for folding potentials where a re-calculation requires to know exactly the used densities (nucleon density or charge density) and the used nucleon-nucleon interaction. In the following, we briefly mention some recent AOMPs and comment on their general properties.

3.7.1 São Paulo potential (2002)

The São Paulo potential (SPP) [85] is intended to describe the nucleus-nucleus interaction for a wide range of colliding nuclei; a recent review celebrated the 20-th birthday of the SPP [86]. The SPP is based on a folding procedure for the real part and various phenomenological parameterizations for the imaginary part. As the SPP is neither optimized for α projectiles nor for low energies, one cannot expect that the SPP is the best choice for the calculation of astrophysical (α,X) reaction rates. Instead, a similar performance as the DEM AOMPs should be achievable for the SPP because the general approach is similar. As for most other AOMPs, the predictions for low-energy cross sections will also be sensitive to the tail of the chosen imaginary part (as discussed above for the MCF AOMP). We note that a computer code for the second version SPP2 of this potential became available a few years ago in [87].

3.7.2 Guo et al. (2011)

Guo et al. [88] provide a fully microscopic AOMP from the Green's function method in combination with an effective Skyrme interaction. It would be very interesting to see how such a fully microscopic approach works for the low sub-Coulomb energies which are most important for the calculation of astrophysical (α,X) reaction rates, but [88] does not yet cover very low energies. Furthermore, it is not possible to use the Guo et al. AOMP without a full repetition of their work; thus, in practice, this AOMP is unfortunately not accessible.

3.7.3 Durant and Capel (2022)

A recent study of the AOMP by Durant and Capel [89] focuses on higher energies between 100 MeV and 400 MeV. As these energies are far above the astrophysically relevant

energy range, we do not provide further discussion of this AOMP here.

3.7.4 Basak and Basu (2022)

The AOMP by Basak and Basu [59] is constructed at low energies. It is based on the MCF AOMP. An additional energy dependence with a Fermi function, see Eq. (13), is introduced, and ranges in the NZ-plane are defined where this energy dependence has to be applied either to the real and imaginary part or to the imaginary part only or not at all. Basak and Basu also point out the major influence of the imaginary potential for the low-energy cross sections. But as we have seen in Sect. 3.3, the energy dependence of the MCF AOMP is mainly an adjustment of the tail of the imaginary part to existing data. Furthermore, the given NZ-ranges for the application of the energy dependence in [59] do not look very systematic. Especially the latter finding does not support this AOMP for the calculation of astrophysical (α,X) reaction rates.

3.7.5 Nhu Le and Quang Hung (2022)

Again similar to the DEM AOMP, the AOMP by Nhu Le and Quang Hong [58] (NLQH) is based on a real folding potential and a WS potential in the imaginary part. The folding potential is based on the CDM3Y1 interaction plus a repulsive potential, and its strength includes a dispersive contribution. The NLQH study focuses on low energies. Similar to previous work, also NLQH conclude that the imaginary part of the potential is essential for the calculation of the (α,n) and (α,γ) cross sections at low energies under study in [58]. Also similar to previous work, an energy dependence of the imaginary part of Fermi type is used to obtain a good reproduction of several (α,n) and (α,γ) data.

It is pointed out in [58] that the results of the NLQH AOMP are close to the AVR AOMP. NLQH favor their approach because of the smaller number of adjustable parameters when compared with the many-parameter AVR AOMP. However, also the NLQH AOMP suffers from the sensitivity to the tail of the imaginary part of the potential.

3.7.6 Denisov (2025)

Contrary to most other above AOMPs, but similar to the Atomki-V2 AOMP, the AOMP by Denisov [90] is based on the barrier transmission approach; i.e., the so-called UMADAC (Unified Model for Alpha-Decay and Alpha-Capture) AOMP is a purely real potential; for earlier work on the UMADAC AOMP, see also [91,92].

The transmission in the Denisov AOMP is tested and verified against α-decay half-lives and α-induced fusion data. Again, this approach is similar to the folding potential in the real part of the Atomki-V2 AOMP which was also applied to α-decay in several previous studies (e.g., [70,93–95]).

Unfortunately, the work by Denisov [90] stops at the calculation of total reaction cross sections σ_{reac} in the barrier transmission approach. No attempt is made to calculate the cross sections of the individual (α,X) exit channels. From the close similarity of the Atomki-V2 and Denisov AOMPs, it can be expected that the introduction of a deep, narrow, and sharp-edged imaginary part (similar to the Atomki-V2 AOMP, see Sect. 3.6) will lead to an excellent performance of the Denisov AOMP for the prediction of low-energy (α,X) cross sections and astrophysical reaction rates.

4 Example: ^{100}Mo + α

4.1 Cross section and S-factor

In the following we present the results from the AOMPs in Sects. 3.3, 3.4, 3.5, and 3.6 for the example of ^{100}Mo + α. This example was chosen because two recent experiments have provided reliable data using either the activation technique for the ^{100}Mo$(\alpha,1n)^{103}$Ru reaction [32] or an active-target technique in inverse kinematics for the sum over ^{100}Mo$(\alpha,xn)^{104\text{-}x}$Ru with $x = 0 - 2$ at the energies under study [33] with $x = 0$ being the (α,γ) reaction.

Figure 6 shows the calculated total reaction cross sections σ_{reac} for the MCF, DEM (3 versions), AVR, and Atomki-V2 AOMPs. Because σ_{reac} covers almost 20 orders of magnitude for the shown energy range, the data are presented as ratio to the result from the Atomki-V2 AOMP. This AOMP is chosen as a reference here because it was also recommended in the two recent experimental studies of ^{100}Mo + α [32,33].

The first interesting result from Fig. 6 is the nice agreement of all AOMPs at energies above the Coulomb barrier. Between 15 MeV and 20 MeV, the deviations between the different AOMPs remain very limited with less than 30% difference between the lowest (DEM-2) and highest (Atomki-V2) σ_{reac}. This is an expected result (as already discussed in Sect. 2.2).

Again expected, the MCF AOMP leads to much higher σ_{reac} towards lower energies. This is explained by the significant contribution from the tail of the imaginary part, see Sect. 3.3 and Fig. 4. The deviation between the MCF and the Atomki-V2 AOMPs exceeds a factor of 50 at the lowest energy of 3 MeV in Fig. 6.

Somewhat surprising, the three versions of the DEM AOMP show completely different results. The DEM-1 AOMP behaves very similar as the MCF AOMP with a steep increase towards low energies, reaching a factor of 25 deviation from Atomki-V2 at 3 MeV. Contrary, the DEM-2 and DEM-3 AOMPs predict lower σ_{reac}. The deviation between the DEM-2 AOMP and the Atomki-V2 AOMP remains small

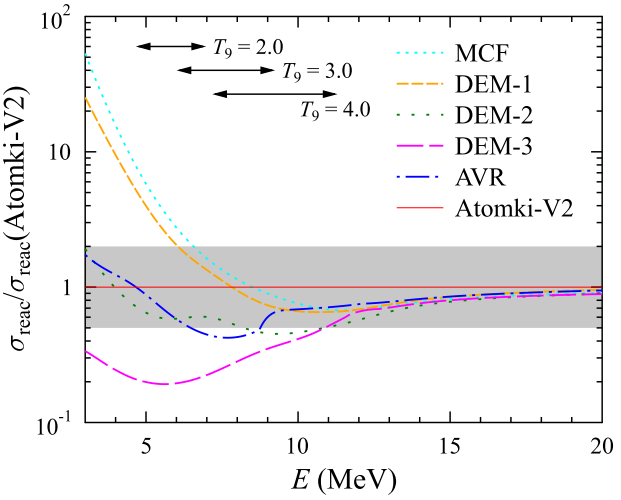

Fig. 6 Ratio $\sigma_{reac}/\sigma_{reac}$(Atomki-V2) for the different AOMPs in Sects. 3.3, 3.4, 3.5, and 3.6: MCF (light-blue short-dotted), DEM-1 (orange short-dashed), DEM-2 (green dotted), DEM-3 (magenta dashed), AVR (blue dash-dotted), and Atomki-V2 (≡1, thin full red line). The light-grey bar indicates the claimed uncertainty of a factor of two for the Atomki-V2 AOMP. The classical Gamow windows for $T_9 = 2$, 3, and 4 are indicated by horizontal arrows. Further discussion see text

(almost within a factor of two for all energies in Fig. 6). The DEM-3 AOMP leads to lower σ_{reac} by a factor of $2-5$ below 10 MeV.

The AVR AOMP remains also close to the Atomki-V2 AOMP, with deviations almost within a factor of two. However, the energy dependence of the AVR prediction shows a surprisingly pronounced structure around 9 MeV.

The grey-shaded band in Fig. 6 indicates the claimed uncertainty of a factor of two for the Atomki-V2 AOMP. The DEM-3 AOMP remains within this uncertainty band only above 10 MeV and is below for lower energies; the DEM1 and MCF AOMPs remain within the uncertainty band down to about $6-7$ MeV and are higher for lower energies. The DEM-2 and AVR AOMPs remain practically inside the uncertainty band at all energies in Fig. 6. Consequences for the astrophysical reaction rate $N_A\langle\sigma v\rangle$ will be discussed later in Sect. 4.2.

Next, we compare the predictions of the various AOMPs to the recent experimental data by Szegedi et al. [32] and Ong et al. [33]. For completeness we also include the earlier data by Graf and Münzel [96] and Esterlund and Pate [97] which have also been obtained by the activation technique. Graf and Münzel used individual targets for each energy whereas Esterlund and Pate applied the stacked-foil technique. As already shown in Fig. 2 of [32], these earlier data sets show some irregularities; this holds in particular for the lowest energy of the stacked-foil experiment where the cross section exceeds the later data by roughly two orders of magnitude.

Figure 7 shows the astrophysical S-factor for the ^{100}Mo(α,1n)^{103}Ru reaction in linear (upper part a) and in logarithmic (lower part b) scale. First of all, we note that the recent experimental data from the activation experiment by Szegedi et al. [32] and from the active-target experiment by Ong et al. [33] are in good agreement within the given error bars below the (α,2n) threshold at 10.8 MeV. The earlier activation data by Graf and Münzel [96] and Esterlund and Pate [97] are somewhat higher around 10 MeV and somewhat lower at higher energies, thus showing a different energy dependence. The lowest data point of Esterlund and Pate at 6.8 MeV exceeds the lowest S-factor by Szegedi et al. by more than two orders of magnitude (outside the shown range in Fig. 7), thus further questioning the energy dependence of the earlier data at low energies.

The linear plot in the upper part of Fig. 7 shows nicely that the energy dependence of the S-factor at low energies is well reproduced by the Atomki-V2 AOMP whereas all other AOMPs under study clearly deviate from the experimental data. The MCF and DEM-1 AOMPs show a much steeper energy dependence, and the DEM-3 AOMP shows a flatter energy dependence. The DEM-2 and AVR AOMPs remain relatively close to the Atomki-V2 AOMP but show surprising structures in the low-energy range (see also Fig. 6). As this is the astrophysically most relevant energy region, we favor the Atomki-V2 AOMP for the calculation of astrophysical reaction rates. This is further comfirmed by a χ^2 analysis of the deviation between the experimental data and prediction from various AOMPs in [32]. The smallest χ^2 was found for the Atomki-V2 AOMP with an overall normalization factor of 1.21 (i.e., close to unity). Larger normalization factors had to be used for the other AOMPs under study, and nevertheless the χ^2 of the Atomki-V2 AOMP could not be reached by the other AOMPs.

At higher energies above the (α,2n) threshold, the active-target data by Ong et al. are higher than the activation data by Szegedi et al. because the active-target experiment detects all $Z \rightarrow Z+2$ events and thus measures the sum over ^{100}Mo(α,xn)$^{104\text{-}x}$Ru cross sections (with $x = 0-2$ in the energy range under study). This is best visible in the cross section plot in Fig. 4 of [33], but also visible in the S-factor plot in the lower part b) of Fig. 7.

At higher energies, the predictions from all AOMPs under study agree, and the predictions also agree at energies above 30 MeV (see the discussion in Sect. 2.2). But the early experimental data by Graf and Münzel [96] and Esterlund and Pate [97] are significantly higher than the predicted (α,n) cross sections above 15 MeV. A better description of the earlier experimental data can be achieved if the calculated branching $b_{1n} \approx T_{1n}/(T_{1n}+T_{2n})$ towards the (α,n) channel is slightly enhanced. This can be achieved by a modified level density in the statistical model, either by enhancing the LD in ^{103}Ru (thus increasing T_{1n}) or decreasing the LD in ^{104}Ru

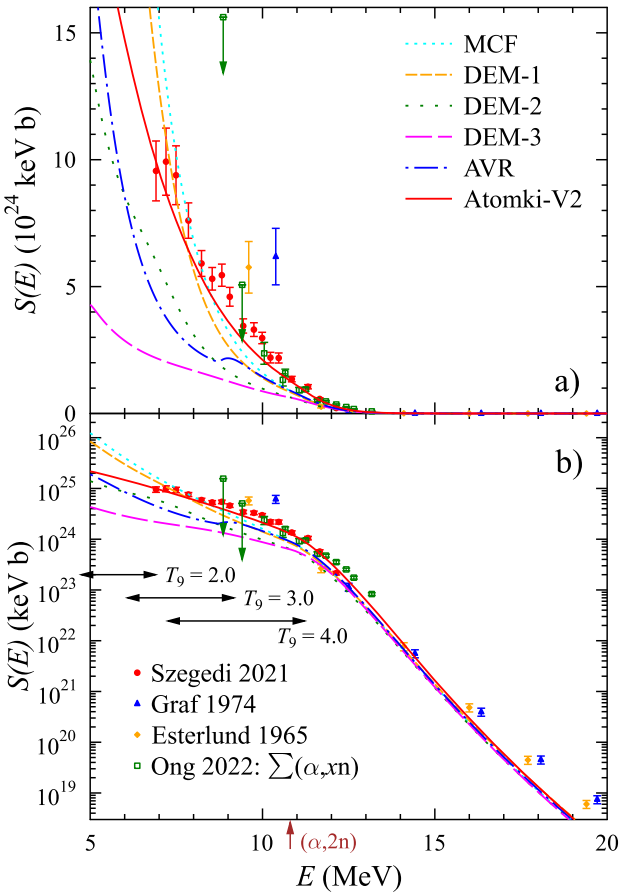

Fig. 7 Cross section of the ^{100}Mo(α,1n)^{103}Ru reaction (shown as astrophysical S-factor) in linear (upper part a) and in logarithmic (lower part b) scale: Comparison of experimental data [32,96,97] to the predictions from the different AOMPs by MCF (light-blue short-dotted), DEM-1 (orange short-dashed), DEM-2 (green dotted), DEM-3 (magenta dashed), AVR (blue dash-dotted), and Atomki-V2 (full red line). The lowest data point of Esterlund and Pate is far above the chosen scale. The data by Ong et al. [33] contain contributions from the ^{100}Mo(α,2n)^{102}Ru reaction above the (α,2n) threshold at 10.8 MeV; the threshold is indicated by a vertical arrow. The classical Gamow windows for $T_9 = 2$, 3, and 4 are shown by horizontal arrows (see Table 3). Further discussion see text

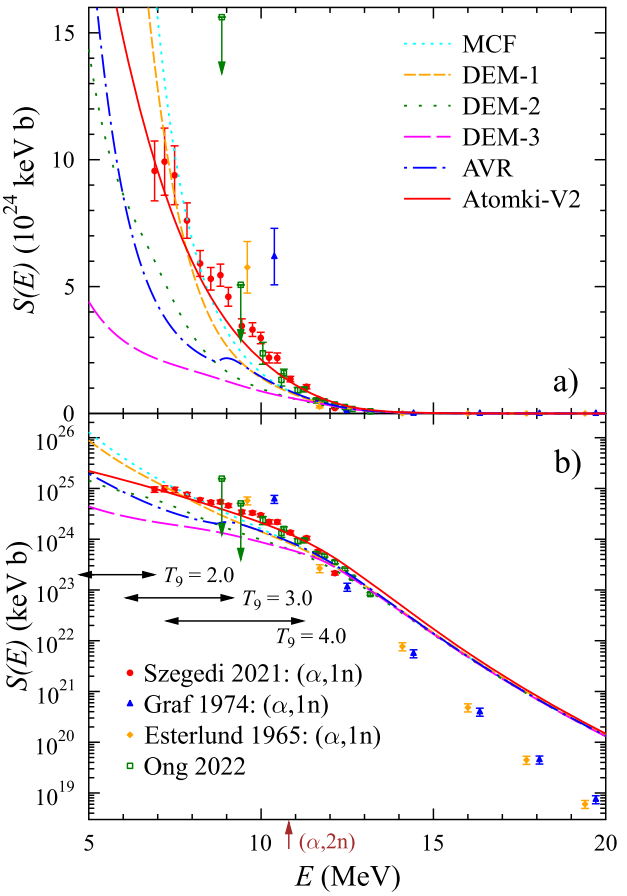

Fig. 8 Cross section of the sum of the ^{100}Mo(α,xn)$^{104\text{-}x}$Ru reactions with $x = 0 - 2$ (shown as astrophysical S-factor) in linear (upper part a) and in logarithmic (lower part b) scale: Comparison of experimental data [33] to the predictions from the different AOMPs by MCF (light-blue short-dotted), DEM-1 (orange short-dashed), DEM-2 (green dotted), DEM-3 (magenta dashed), AVR (blue dash-dotted), and Atomki-V2 (full red line). The activation data [32,96,97] for the ^{100}Mo(α,1n)^{103}Ru reaction are almost identical to the summed cross section below the (α,2n) threshold which is indicated by a vertical arrow. The classical Gamow windows for $T_9 = 2$, 3, and 4 are shown by horizontal arrows (see Table 3). Further discussion see text

(thus reducing T_{2n}). As these energies are above the astrophysically relevant energy range, no attempts have been made here to optimize the calculations.

Figure 8 is essentially a repetition of Fig. 7 for the sum of the ^{100}Mo(α,xn)$^{104\text{-}x}$Ru cross sections with $x = 0 - 2$. One can see the much higher calculated cross sections from all AOMPs at energies above the (α,2n) threshold at 10.8 MeV. The data at low energies below the (α,2n) threshold are practically not affected because the ^{100}Mo(α,γ)^{104}Ru channel (corresponding $x = 0$) is practically negligible above the (α,1n) threshold at 4.57 MeV (see also Fig. 1).

4.2 Astrophysical reaction rate

After the discussion of the reaction cross sections, we now turn to the calculation of astrophysical reaction rates $N_A \langle \sigma v \rangle$ for ^{100}Mo + α. Two explosive scenarios (γ-process and weak r-process) have been mentioned in the introduction where α-induced reactions on heavy target nuclei are relevant for the reaction path. Consequently, it is important to provide the reaction rates for explosive scenarios at relatively high temperatures at least above $T_9 = 1$.

^{100}Mo is located at the "east" end of the stable molybdenum isotopes on the chart of nuclides; i.e., for this example of ^{100}Mo we are mainly interested in the relevant rates for the weak r-process. Here the important astrophysical rate is

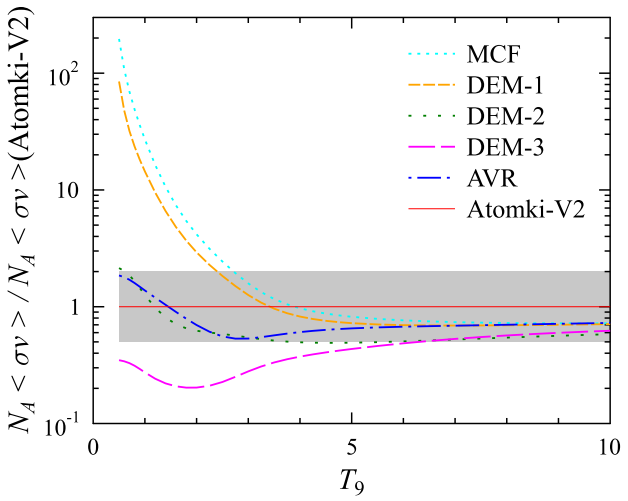

Fig. 9 Astrophysical reaction rate of the $Z \rightarrow Z+2$ reaction which produces ruthenium isotopes $^{104\text{-x}}$Ru from the ^{100}Mo(α,xn)$^{104\text{-x}}$Ru reactions (normalized to the rate from the Atomki-V2 AOMP). The predictions from the various AOMPs under study differ in particular towards lower temperatures: MCF (light-blue short-dotted), DEM-1 (orange short-dashed), DEM-2 (green dotted), DEM-3 (magenta dashed), AVR (blue dash-dotted), and Atomki-V2 ($\equiv$1, thin full red line). The grey-shaded area represents the claimed uncertainty of the Atomki-V2 AOMP. The calculations stop at $T_{9,\min} = 0.5$ because the rates become negligibly small at lower temperatures. Further discussion see text

the overall transition rate from a nucleus with charge number Z to $Z+2$. It plays only a minor role which of the ^{100}Mo(α,xn)$^{104\text{-x}}$Ru reactions has occurred because the high temperatures in combination with the high neutron densities lead to a (n,γ)-(γ,n) equilibrium. Simply speaking: whatever ruthenium isotope is produced by ^{100}Mo(α,xn) is not really relevant because the abundances of the individual ruthenium isotopes approach their equilibrium distribution by (n,γ) and (γ,n) reactions in a short timescale. The equilibrium distribution depends only on the neutron binding energies, but not on the production path. Figure 9 shows the $Z \rightarrow Z+2$ reaction rates for the various AOMPs under study which is the sum over the ^{100}Mo(α,xn)$^{104\text{-x}}$Ru reaction rates. Following the discussion in Sect. 2.1, we point out that this $Z \rightarrow Z+2$ rate is essentially governed by the AOMP, but is almost insensitive to the other ingredients of the statistical model.

The overestimation of the cross sections by the MCF and DEM-1 AOMPs at low energies leads to dramatically increased reaction rates $N_A \langle \sigma v \rangle$. This is most pronounced towards low temperatures below $T_9 \approx 2$, reaching roughly two orders of magnitude around $T_9 = 0.5$ at the lower end of the present investigation. The DEM-2 and AVR AOMPs predict cross sections lower than the Atomki-V2 AOMP at all shown energies in Figs. 7 and 8. This leads to lower $N_A \langle \sigma v \rangle$ below $T_9 \approx 1.5$, but because of the steep increase of the S-factor towards lower energies for the DEM-2 and AVR AOMPs, the resulting $N_A \langle \sigma v \rangle$ exceed the $N_A \langle \sigma v \rangle$ from the Atomki-V2 AOMP at very low temperatures. The DEM-3 AOMP predicts a lower $N_A \langle \sigma v \rangle$ than Atomki-V2 at all temperatures. It has to be pointed out again that the steep increase of the S-factor towards low energies which is responsible for the increased $N_A \langle \sigma v \rangle$ at low temperatures, results from the tail of the imaginary parts of the respective AOMPs (MCF, DEM-1, DEM-2, AVR).

The astrophysical rates $N_A \langle \sigma v \rangle$ are well constrained by the experimental data of [32,33] down to temperatures of about $T_9 \approx 3$. Below temperatures of $T_9 \approx 2$, the Gamow window is not reached by experiment. Here $N_A \langle \sigma v \rangle$ has to be taken from the AOMP calculations.

Although we have pointed out above that the astrophysically relevant rate is $N_A \langle \sigma v \rangle$ for $Z \rightarrow Z+2$, we disentangle the contributions of the various ^{100}Mo(α,xn) $^{104\text{-x}}$Ru reactions in Fig. 10 because often there is no clear distinction between the inclusive $Z \rightarrow Z+2$ rate and the exclusive (α,1n) rate. E.g., the widely used NON-SMOKER code [55] does not take into account multiple particle emission and thus provides the $Z \rightarrow Z+2$ rate as (α,n) rate. This is also adopted for the REACLIB database [56]. Contrary, the STARLIB database [98] provides the (α,1n) rate from TALYS as (α,n) rate. This may lead to dramatic misunderstandings if not taken into account properly in the subsequent nucleosynthesis networks.

Figure 10 shows that the total $Z \rightarrow Z+2$ rate for ^{100}Mo + α is dominated by the ^{100}Mo(α,γ)^{104}Ru reaction below $T_9 \approx 1$. At these very low temperatures, the Gamow window for the ^{100}Mo + α system is located below the threshold of the (α,n) reaction at $E = 4.57$ MeV, and thus the relevance of the (α,n) reaction becomes marginal. At higher temperatures between $T_9 \approx 2-6$ the ^{100}Mo(α,1n)^{103}Ru reaction dominates the $Z \rightarrow Z+2$ reaction rate, and at extreme temperatures above $T_9 \approx 7$ the ^{100}Mo(α,2n)^{102}Ru contribution with its threshold at 10.8 MeV becomes dominant, even complemented by the ^{100}Mo(α,3n)^{101}Ru reaction. All proton-emitting reactions (summarized as $Z \rightarrow Z+1$ rate) are completely negligible for all relevant temperatures.

It is trivial that the contributions of the different (α,xn) reactions depend sensitively on the thresholds or Q-values of the respective reactions which are significantly negative for (α,1n) reactions around stability. Of course, the Q-value becomes more negative (less negative) towards neutron-deficient (neutron-rich) target nuclei. For illustration we repeat Fig. 10 for the neutron-deficient p-nucleus ^{92}Mo and the slightly neutron-rich and unstable nucleus ^{104}Mo in Fig. 11.

Because of the strongly negative Q-value of the ^{92}Mo(α,n)^{95}Ru reaction of $Q = -9.00$ MeV, the $Z \rightarrow Z+2$ rate for ^{92}Mo + α is dominated by the ^{92}Mo(α,γ)^{106}Ru reaction up to about $T_9 \approx 3$. Only at high temperatures above $T_9 \approx 5$ the ^{92}Mo(α,n)^{95}Ru reaction dominates, and

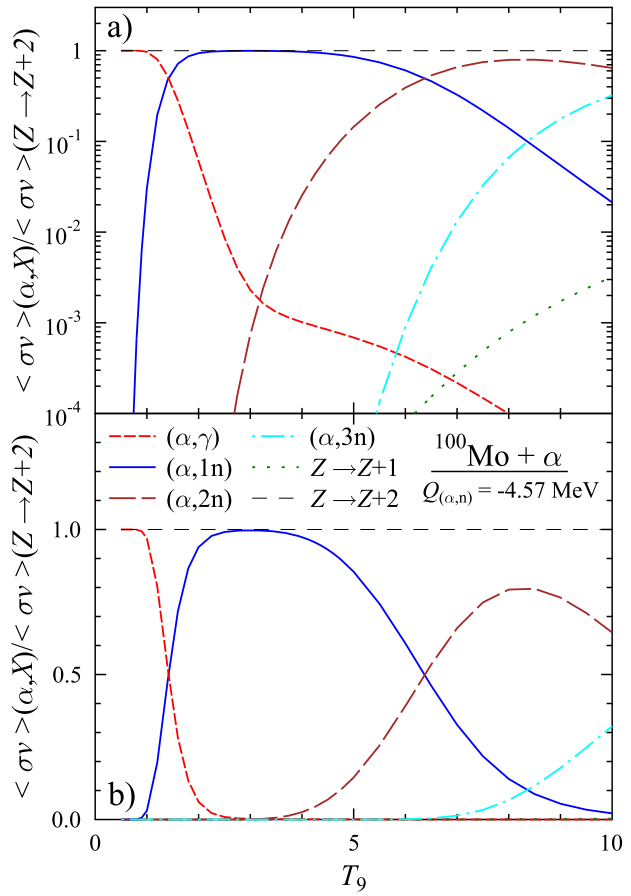

Fig. 10 Ratio of the astrophysical reaction rate $N_A \langle \sigma v \rangle$ of different (α,X) reactions over the total $Z \rightarrow Z+2$ rate for ^{100}Mo + α in logarithmic scale (upper part a) and in linear scale (lower part b). The $Z \rightarrow Z+2$ rate is dominated by the (α,γ) reaction below $T_9 \approx 1$ (red dashed), by the $(\alpha,1n)$ reaction between $T_9 \approx 2-6$ (blue full line), and by the $(\alpha,2n)$ reaction above $T_9 \approx 7$ (brown long-dashed). Further discussion see text

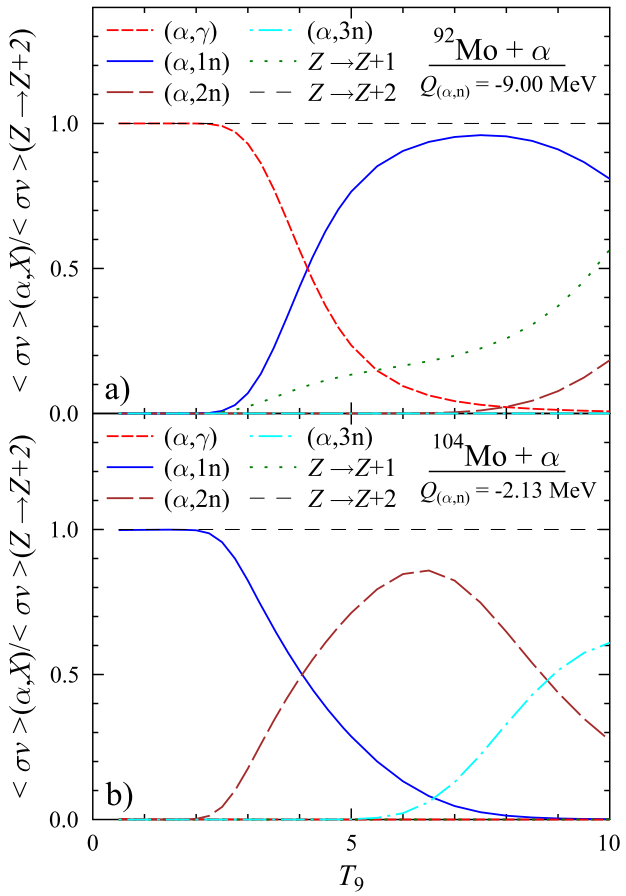

Fig. 11 Ratio of the astrophysical reaction rate $N_A \langle \sigma v \rangle$ of different (α,X) reactions over the total $Z \rightarrow Z+2$ rate for ^{92}Mo + α (upper part a) and ^{104}Mo + α (lower part b). For the neutron-deficient ^{92}Mo the dominating reactions are ^{92}Mo$(\alpha,\gamma)^{96}$Ru at low temperatures and ^{92}Mo$(\alpha,1n)^{95}$Ru at high temperatures with a small additional contribution of the ^{92}Mo$(\alpha,p)^{95}$Tc reaction. Contrary, for the moderately neutron-rich ^{104}Mo the dominating reactions are ^{104}Mo$(\alpha,1n)^{107}$Ru and ^{104}Mo$(\alpha,2n)^{106}$Ru with a significant contribution of ^{104}Mo$(\alpha,3n)^{105}$Ru at the highest temperatures. Further discussion see text

also some contribution from the ^{92}Mo$(\alpha,p)^{95}$Tc reaction can be seen in Fig. 11; this contribution is shown as summed $Z \rightarrow Z+1$ rate which includes also a tiny contribution of the (α,pn) reaction.

The situation changes dramatically for the moderately neutron-rich ^{104}Mo. The Q-value of the ^{104}Mo$(\alpha,n)^{107}$Ru reaction is only slightly negative with $Q = -2.13$ MeV, and thus the Gamow window for ^{104}Mo + α is located completely above the (α,n) threshold for temperatures above $T_9 \approx 1$. As a consequence, the ^{104}Mo$(\alpha,\gamma)^{108}$Ru reaction becomes completely negligible, and already at the lowest temperatures under study the ^{104}Mo$(\alpha,1n)^{107}$Ru reaction defines the $Z \rightarrow Z+2$ rate. At $T_9 \approx 4$, the contributions of the $(\alpha,1n)$ and the $(\alpha,2n)$ reactions become equal, and at extreme temperatures above $T_9 \approx 7$ also the ^{104}Mo$(\alpha,3n)^{105}$Ru reaction is a non-negligible contributor to the $Z \rightarrow Z+2$ rate. This clearly shows that the role of $(\alpha,2n)$ and $(\alpha,3n)$ reactions has to be taken into account at least for neutron-rich target nuclei several mass units "east" of stability.

The results in Figs. 10 and 11 have been obtained from the Atomki-V2 AOMP. Results from the other AOMPs would not be much different because the branching ratios b_X are governed by the Q-values and by the other ingredients of the statistical model (see Sect. 2.1).

5 Discussion

Two essential results can be extracted from the above presentation of the different AOMPs and the comparison to the experimental data for the chosen example of ^{100}Mo + α. Further examples will be mentioned later after the discussion of the main results.

First, the reason for the huge range of predictions for the (α,X) cross sections at low energies and the resulting huge range of predictions for the astrophysical reaction rates $N_A\langle\sigma v\rangle$ is now understood. It results from the tiny tail of the imaginary part of the AOMP at large radii (outside the colliding nuclei, with a potential depth of the order of 0.1% of the central depth or even below). Although it has been pointed out in many previous studies that the calculated (α,X) cross sections are very sensitive to the imaginary part of the AOMP, it was not realized until [48,67] that this sensitivity results mainly from the tail of the imaginary part.

The real and imaginary parts of the AOMP are often derived from the analysis of elastic scattering. However, such an analysis is mainly sensitive to the nuclear surface, but cannot constrain the tail of the imaginary part at large radii. In practice the tail of the imaginary part results – more or less by accident – from the chosen parameterization of the AOMP (WS in the most cases). Often an energy dependence of the strength of the imaginary part is introduced to reproduce experimental (α,X) data. This energy dependence is mainly a numerical fine-tuning of the tail of the imaginary part. Any physical interpretation of this energy dependence must remain somewhat questionable.

The second essential result is that the uncertainties from the imaginary part of the AOMP can be avoided as soon as the calculation of the total reaction cross section $\sigma_{\rm reac}$ is made in the barrier transmission model (instead of the optical model). $\sigma_{\rm reac}$ in the barrier transmission model results from the transmission through the Coulomb barrier in a purely real potential, and it is implicitly assumed that any incoming α particle is absorbed and contributes to $\sigma_{\rm reac}$ as soon as the barrier is passed.

For practical reasons, the results of the barrier transmission model can be simulated in the optical model by the addition of an imaginary part which is deep, narrow, and sharp-edged. This mimics the implicit assumption of the barrier transmission model that all tunneled α particles are absorbed. Returning to the OM provides the benefit that the widely used standard codes for the calculation of reaction cross sections and astrophysical reaction rates (like e.g. TALYS) can be used without major modifications. The Atomki-V2 AOMP (see Sect. 3.6) is constructed according to these considerations. It is completely determined by the analysis of elastic scattering data [30]; no adjustment of parameters to (α,X) data is required for the Atomki-V2 AOMP.

The analysis of the ^{100}Mo + α data in Sect. 4 clearly shows that the Atomki-V2 AOMP is able to predict the (α,X) cross sections with small uncertainties. Many tests have been made on the uncertainties for the predicted cross sections in the Supplement of [48]. Finally, it is concluded that the predictions are robust within a factor of two or better. This is verified for a series of experimental data for heavy targets in [48], and this finding was confirmed for almost all later experimental data for ^{86}Kr [99], ^{87}Rb [100], ^{96}Zr [101], ^{100}Mo [32,33], $^{120\text{-}130}$Te [72], and ^{144}Sm [102] with the peculiar exception of ^{88}Sr [84].

The experimental ^{88}Sr$(\alpha,n)^{91}$Zr data by Fougères et al. [84] are lower by a factor of about 3 than the prediction from the Atomki-V2 AOMP. This holds for the whole energy range of the experimental data between about 8 MeV and 13 MeV. Also other AOMPs cannot reproduce these experimental data. And also in the systematics of reduced cross sections $\sigma_{\rm red}$ vs. reduced energies $E_{\rm red}$ [41], the ^{88}Sr data appear as outliers, about a factor of 3 lower than the data for neighboring nuclei (see Figs. 4 and 5 of [84]). Because of this peculiar behavior of ^{88}Sr, many checks have been made in the analysis of [84], and the experiment was partly repeated, confirming the results. Therefore, in the meantime angular distributions of ^{88}Sr$(\alpha,\alpha)^{88}$Sr elastic scattering were measured at Atomki, and it is planned to derive the total reaction cross sections $\sigma_{\rm reac}$ from three angular distributions between 13 MeV and 20 MeV; i.e., there is overlap with the ^{88}Sr$(\alpha,n)^{91}$Zr data in [84]. It will be very interesting to see whether $\sigma_{\rm reac}$ from elastic scattering will agree with the cross section of the ^{88}Sr$(\alpha,n)^{91}$Zr reaction around 13 MeV. Unfortunately, the analysis of the ^{88}Sr$(\alpha,\alpha)^{88}$Sr scattering data is not yet completed.

The reaction rates $N_A\langle\sigma v\rangle$ of α-induced reactions for target nuclei between iron ($Z = 26$) and bismuth ($Z = 83$) were calculated from the Atomki-V2 AOMP [49]. Numerical tables are available at the publisher of [49] with open access. The new reaction rates with their smaller uncertainties have been applied to a calculation of the nucleosynthesis in the weak r-process [103]. Previous nucleosynthesis calculations used much larger uncertainties for the α-induced reactions in the weak r-process [11,12]. At least one order of magnitude was estimated in [11], similar to the estimates for the uncertainties of (α,γ) rates in the γ-process [20,21]. It is shown in [103] that the smaller uncertainties from the Atomki-V2 AOMP lead to acceptable uncertainties of the resulting nucleosynthesis. Now the nuclear uncertainties of calculated abundance ratios are comparable to the observational uncertainties which allows to draw stronger conclusions on the astrophysical conditions of the weak r-process. The larger uncertainties of one order of magnitude or more for the α-induced reactions in previous work showed a huge spread in the calculated nucleosynthesis yields and abundance ratios, thus not allowing to draw firm conclusions on the astrophysical conditions. As soon as experimental data allow to reduce the uncertainties further, even stricter constraints will be possible; see e.g. the discussion in [101] for the ^{96}Zr$(\alpha,n)^{99}$Mo reaction.

The Atomki-V2 AOMP provides a major step ahead for the reliable calculation of astrophysical reaction rates $N_A\langle\sigma v\rangle$ for α-induced reactions. But still further improvements are possible. The Atomki-V2 AOMP (as all folding

potentials) depends on the underlying nuclear densities and on the chosen nucleon-nucleon interaction in Eq. (11). Any progress here is welcome. One option could be the consistent description of the interaction and the resulting densities from a relativistic mean field approach as e.g. suggested in [104]. Furthermore, deformation could be included, and a coupled-channels approach could replace the simple barrier transmission model. However, for consistency this requires a complete re-determination of the AOMP by refitting all angular distributions; simply adding deformation to an existing spherically symmetric potential would double-count the relevance of deformation (see Sect. 3.1).

6 Summary and conclusions

The present study reviews the available α-nucleus optical model potentials with a focus on the AOMPs by McFadden and Satchler [45], Demetriou et al. [46], Avrigeanu et al. [47], and Atomki-V2 [48]. The huge range of predictions for low-energy cross sections and for the astrophysical reaction rates $N_A \langle \sigma v \rangle$ from the different AOMPs under study is explained by the importance of the poorly constrained tail of the imaginary part of the AOMP at large radii (outside the colliding nuclei). The new Atomki-V2 AOMP avoids these complications by the determination of the total reaction cross sections σ_{reac} from the barrier transmission model (instead of the optical model with the inherent uncertainties of the imaginary part of the potential).

Cross sections and reaction rates for the chosen example ^{100}Mo + α are analyzed in detail. It is found that the Atomki-V2 AOMP provides an excellent prediction of all (α,X) cross sections under study down to the lowest energies. Typical uncertainties are reduced to less than a factor of two whereas previously much larger uncertainties had to be used in nucleosynthesis calculations [11,20,21,103]. This excellent performance of the Atomki-V2 AOMP is also verified for many other heavy target nuclei (with one exception for ^{88}Sr [84]). Further tests should also cover α-induced reactions on unstable targets (typically measured in inverse kinematics with a heavy projectile and an active ^{4}He target system). Such experiments are planned for the near future. The predictions from the Atomki-V2 AOMP have been provided to the investigators for the proposals, and these predictions were used for the countrate estimates. Finally, the best verification of an AOMP results from the combination of data along isotopic or isotonic chains with high-precision data for the stable isotopes and best achievable precision for the unstable isotopes.

The smaller uncertainties of the reaction rates from the Atomki-V2 AOMP allow to draw stronger conclusions on astrophysical conditions. This opens the door for new astrophysical results. E.g., for the weak r-process it becomes possible to constrain the astrophysical conditions from a comparison of observed abundance ratios to the results of a nucleosynthesis calculation [103].

Note added in proof: During review of the present study, a first experimental result for an (α,n) cross section of an unstable nucleus in the weak r-process was published, see M. Williams et al., Phys. Rev. Lett. **134**, 112701 (2025). It will be interesting to see how the measured partial ^{94}Sr(α,$n\gamma_{407}$)^{97}Zr cross section is able to further constrain the AOMPs under investigation.

Acknowledgements We thank our colleague and friend Endre Somorjai who initiated this project more than 30 years ago and has encouraged us by his enthusiasm for research over all the years. This work was supported by NKFIH (K134197, K147010).

Data Availability Statement Data will be made available on reasonable request. [Authors' comment: The datasets generated during and/or analysed during the current study are available from the corresponding author on reasonable request.]

Code Availability Statement Code/software will be made available on reasonable request. [Authors' comment: The code/software generated during and/or analysed during the current study is available from the corresponding author on reasonable request.]

References

1. A. Coc, E. Vangioni, Primordial nucleosynthesis. International Journal of Modern Physics E **26**(08), 1741002 (2017). https://doi.org/10.1142/S0218301317410026
2. E.G. Adelberger, A. García, R. Robertson, K.A. Snover, A.B. Balantekin, K. Heeger, M.J. Ramsey-Musolf, D. Bemmerer, A. Junghans, C.A. Bertulani, J.-W. Chen, H. Costantini, P. Prati, M. Couder, E. Uberseder, M. Wiescher, R. Cyburt, B. Davids, S.J. Freedman, M. Gai, D. Gazit, L. Gialanella, G. Imbriani, U. Greife, M. Hass, W.C. Haxton, T. Itahashi, K. Kubodera, K. Langanke, D. Leitner, M. Leitner, P. Vetter, L. Winslow, L.E. Marcucci, T. Motobayashi, A. Mukhamedzhanov, R.E. Tribble, K.M. Nollett, F.M. Nunes, T.-S. Park, P.D. Parker, R. Schiavilla, E.C. Simpson, C. Spitaleri, F. Strieder, H.-P. Trautvetter, K. Suemmerer, S. Typel, Solar fusion cross sections. ii. the *pp* chain and CNO cycles. Rev. Mod. Phys. **83**, 195–245 (2011). https://doi.org/10.1103/RevModPhys.83.195
3. D. Dunbar, R.E. Pixley, W.A. Wenzel, W. Whaling, The 7.68-Mev state in C^{12}. Phys. Rev. **92**, 649–650 (1953). https://doi.org/10.1103/PhysRev.92.649

4. F. Hoyle, On Nuclear Reactions Occuring in Very Hot STARS. I. the Synthesis of Elements from Carbon to Nickel. Astroph. J. Suppl. **1**, 121 (1954). https://doi.org/10.1086/190005
5. E.G. Adelberger, A. García, R. Robertson, K.A. Snover, A.B. Balantekin, K. Heeger, M.J. Ramsey-Musolf, D. Bemmerer, A. Junghans, C.A. Bertulani, J.-W. Chen, H. Costantini, P. Prati, M. Couder, E. Uberseder, M. Wiescher, R. Cyburt, B. Davids, S.J. Freedman, M. Gai, D. Gazit, L. Gialanella, G. Imbriani, U. Greife, M. Hass, W.C. Haxton, T. Itahashi, K. Kubodera, K. Langanke, D. Leitner, M. Leitner, P. Vetter, L. Winslow, L.E. Marcucci, T. Motobayashi, A. Mukhamedzhanov, R.E. Tribble, K.M. Nollett, F.M. Nunes, T.-S. Park, P.D. Parker, R. Schiavilla, E.C. Simpson, C. Spitaleri, F. Strieder, H.-P. Trautvetter, K. Suemmerer, S. Typel, Solar fusion cross sections. ii. the *pp* chain and CNO cycles. Rev. Mod. Phys. **83**, 195–245 (2011). https://doi.org/10.1103/RevModPhys.83.195
6. H. Schatz, K.E. Rehm, X-ray binaries. Nucl. Phys. A **777**, 601–622 (2006). https://doi.org/10.1016/j.nuclphysa.2005.05.200. (**Special Isseu on Nuclear Astrophysics**)
7. A. Parikh, J. José, F. Moreno, C. Iliadis, The effects of variations in nuclear processes on type I X-ray burst nucleosynthesis. Astrophys. J. Suppl. Ser. **178**(1), 110 (2008). https://doi.org/10.1086/589879
8. M. Lugaro, M. Pignatari, R. Reifarth, M. Wiescher, The s process and beyond. Annual Review of Nuclear and Particle Science 73(Volume 73, 2023), 315–340 (2023). https://doi.org/10.1146/annurev-nucl-102422-080857
9. F. Käppeler, R. Gallino, S. Bisterzo, W. Aoki, The *s* process: Nuclear physics, stellar models, and observations. Rev. Mod. Phys. **83**, 157–193 (2011). https://doi.org/10.1103/RevModPhys.83.157
10. W. Hauser, H. Feshbach, The inelastic scattering of neutrons. Phys. Rev. **87**, 366–373 (1952). https://doi.org/10.1103/PhysRev.87.366
11. J. Pereira, F. Montes, Theoretical uncertainty of (α, n) reactions relevant for the nucleosynthesis of light r-process nuclei in neutrino-driven winds. Phys. Rev. C **93**, 034611 (2016). https://doi.org/10.1103/PhysRevC.93.034611
12. P. Mohr, Role of (α, n) reactions under r-process conditions in neutrino-driven winds reexamined. Phys. Rev. C **94**, 035801 (2016). https://doi.org/10.1103/PhysRevC.94.035801
13. J. Bliss, A. Arcones, F. Montes, J. Pereira, Impact of $(\alpha$, n) reactions on weak r-process in neutrino-driven winds. J. Phys. G: Nucl. Part. Phys. **44**(5), 054003 (2017). https://doi.org/10.1088/1361-6471/aa63bd
14. J. Bliss, A. Arcones, F. Montes, J. Pereira, Nuclear physics uncertainties in neutrino-driven, neutron-rich supernova ejecta. Phys. Rev. C **101**, 055807 (2020). https://doi.org/10.1103/PhysRevC.101.055807
15. S.E. Woosley, W.M. Howard, The p-process in supernovae. Astroph. J. Suppl. **36**, 285–304 (1978). https://doi.org/10.1086/190501
16. M. Arnould, S. Goriely, The p-process of stellar nucleosynthesis: astrophysics and nuclear physics status. Phys. Rep. **384**(1), 1–84 (2003). https://doi.org/10.1016/S0370-1573(03)00242-4
17. D.L. Lambert, The p-nuclei: abundances and origins. Astronomy and Astrophysics Reviews **3**(3–4), 201–256 (1992). https://doi.org/10.1007/BF00872527
18. T. Rauscher, N. Dauphas, I. Dillmann, C. Fröhlich, Z. Fülöp, G. Gyürky, Constraining the astrophysical origin of the p-nuclei through nuclear physics and meteoritic data. Rep. Prog. Phys. **76**(6), 066201 (2013). https://doi.org/10.1088/0034-4885/76/6/066201
19. M. Pignatari, K. Göbel, R. Reifarth, C. Travaglio, The production of proton-rich isotopes beyond iron: The γ-process in stars. International Journal of Modern Physics E **25**(04), 1630003 (2016). https://doi.org/10.1142/S0218301316300034
20. T. Rauscher, N. Nishimura, R. Hirschi, G. Cescutti, A. Murphy, A. Heger, Uncertainties in the production of p nuclei in massive stars obtained from Monte Carlo variations. Mon. Not. R. Astron. Soc. **463**(4), 4153–4166 (2016). https://doi.org/10.1093/mnras/stw2266
21. N. Nishimura, T. Rauscher, R. Hirschi, A.S.J. Murphy, G. Cescutti, C. Travaglio, Uncertainties in the production of p nuclides in thermonuclear supernovae determined by Monte Carlo variations. Monthly Notices of the Royal Astronomical Society **474**(3), 3133–3139 (2017) https://doi.org/10.1093/mnras/stx3033http://oup.prod.sis.lan/mnras/article-pdf/474/3/3133/22892024/stx3033.pdf
22. N. Bohr, Neutron Capture and Nuclear Constitution. Nature **137**, 344–348 (1936). https://doi.org/10.1038/137344a0
23. V.F. Weisskopf, D.H. Ewing, On the yield of nuclear reactions with heavy elements. Phys. Rev. **57**, 472–485 (1940). https://doi.org/10.1103/PhysRev.57.472
24. P.A. Moldauer, Evaluation of the fluctuation enhancement factor. Phys. Rev. C **14**, 764–766 (1976). https://doi.org/10.1103/PhysRevC.14.764
25. T. Rauscher, The path to improved reaction rates for astrophysics. International Journal of Modern Physics E **20**(05), 1071–1169 (2011). https://doi.org/10.1142/S021830131101840X
26. P. Mohr, R. Talwar, M.L. Avila, Cross sections of α-induced reactions slightly below doubly magic ^{40}Ca from the statistical model. Phys. Rev. C **98**, 045805 (2018). https://doi.org/10.1103/PhysRevC.98.045805
27. T. Rauscher, F.-K. Thielemann, Astrophysical reaction rates from statistical model calculations. At. Data Nucl. Data Tables **75**(1), 1–351 (2000). https://doi.org/10.1006/adnd.2000.0834
28. P. Mohr, F. Käppeler, R. Gallino, Survival of nature's rarest isotope ^{180}Ta under stellar conditions. Phys. Rev. C **75**, 012802 (2007). https://doi.org/10.1103/PhysRevC.75.012802
29. P. Mohr, C. Angulo, P. Descouvemont, H. Utsunomiya, Relation between the ^{16}O$(\alpha,\gamma)^{20}$Ne reaction and its reverse ^{20}Ne$(\gamma,\alpha)^{16}$O reaction in stars and in the laboratory. The European Physical Journal A **27**(1), 75–78 (2006). https://doi.org/10.1140/epja/i2006-08-010-1
30. P. Mohr, G.G. Kiss, Z. Fülöp, D. Galaviz, G. Gyürky, E. Somorjai, Elastic alpha scattering experiments and the alpha-nucleus optical potential at low energies. At. Data Nucl. Data Tables **99**(6), 651–679 (2013). https://doi.org/10.1016/j.adt.2012.10.003
31. P. Mohr, Total reaction cross section of light stable and exotic nuclei on lead at energies around the Coulomb barrier. The European Physical Journal A **60**(9), 193 (2024). https://doi.org/10.1140/epja/s10050-024-01403-6
32. T.N. Szegedi, G.G. Kiss, P. Mohr, A. Psaltis, M. Jacobi, G.G. Barnaföldi, T. Szücs, G. Gyürky, A. Arcones, Activation thick target yield measurement of ^{100}Mo$(\alpha, n)^{103}$Ru for studying the weak r-process nucleosynthesis. Phys. Rev. C **104**, 035804 (2021). https://doi.org/10.1103/PhysRevC.104.035804
33. W.-J. Ong, M.L. Avila, P. Mohr, K.E. Rehm, D. Santiago-Gonzalez, J. Chen, C.R. Hoffman, Z. Meisel, F. Montes, J. Pereira, Measurement of the ^{100}Mo(α, xn) cross section at weak r-process energies. Phys. Rev. C **105**, 055803 (2022). https://doi.org/10.1103/PhysRevC.105.055803
34. P. Mohr, T. Rauscher, H. Oberhummer, Z. Máté, Z. Fülöp, E. Somorjai, M. Jaeger, G. Staudt, ^{144}Sm-α optical potential at astrophysically relevant energies derived from ^{144}Sm$(\alpha, \alpha)^{144}$Sm elastic scattering. Phys. Rev. C **55**, 1523–1531 (1997). https://doi.org/10.1103/PhysRevC.55.1523
35. N. Otuka, Data base EXFOR. https://www-nds.iaea.org/exfor/
36. N. Otuka, E. Dupont, V. Semkova, B. Pritychenko, A.I. Blokhin, M. Aikawa, S. Babykina, M. Bossant, G. Chen, S. Dunaeva,

R.A. Forrest, T. Fukahori, N. Furutachi, S. Ganesan, Z. Ge, O.O. Gritzay, M. Herman, S. Hlavač, K. Katō, B. Lalremruata, Y.O. Lee, A. Makinaga, K. Matsumoto, M. Mikhaylyukova, G. Pikulina, V.G. Pronyaev, A. Saxena, O. Schwerer, S.P. Simakov, N. Soppera, R. Suzuki, S. Takács, X. Tao, S. Taova, F. Tárkányi, V.V. Varlamov, J. Wang, S.C. Yang, V. Zerkin, Y. Zhuang, Towards a More Complete and Accurate Experimental Nuclear Reaction Data Library (EXFOR): International Collaboration Between Nuclear Reaction Data Centres (NRDC). Nucl. Data Sheets **120**, 272–276 (2014). https://doi.org/10.1016/j.nds.2014.07.065

37. K. Matsuda, Y. Awaya, N. Nakanishi, S. Takeda, Elastic and inelastic scattering of alpha-particles from even mass molybdenum isotopes. J. Phys. Soc. Jpn. **33**(2), 298–303 (1972). https://doi.org/10.1143/JPSJ.33.298
38. S.J. Burger, G. Heymann, Alpha-particle and proton scattering from even mass molybdenum isotopes. Nucl. Phys. A **243**(3), 461–491 (1975). https://doi.org/10.1016/0375-9474(75)90290-0
39. V.V. Gontchar, B.A. Shilyaev, K.S. Zheltonog, A.V. Yushkov, G.N. Ivanov, The study of the structure of molybdenum nuclei by the method of diffraction scattering of alpha particles. Voprosy Atomn. Nauki i Tekhniki, Ser. Fiz. Yad. Reak. **1**, 7 (1977)
40. V. Chisté, R. Lichtenthäler, A. Villari, L.C. Gomes, S-matrix analysis of heavy-ion elastic scattering. Phys. Rev. C **54**, 784–790 (1996). https://doi.org/10.1103/PhysRevC.54.784
41. P. Gomes, J. Lubian, I. Padron, R.M. Anjos, Uncertainties in the comparison of fusion and reaction cross sections of different systems involving weakly bound nuclei. Phys. Rev. C **71**, 017601 (2005). https://doi.org/10.1103/PhysRevC.71.017601
42. U. Atzrott, P. Mohr, H. Abele, C. Hillenmayer, G. Staudt, Uniform α-nucleus potential in a wide range of masses and energies. Phys. Rev. C **53**, 1336–1347 (1996). https://doi.org/10.1103/PhysRevC.53.1336
43. A.J. Koning, S. Hilaire, S. Goriely, computer code TALYS (2017). http://www.talys.eu/
44. A.J. Koning, S. Hilaire, M.C. Duijvestijn, Talys. In: O. Bersillon, F. Gunsing, E. Bauge, R. Jacqmin (eds.) Proceedings of the International Conference on Nuclear Data for Science and Technology, pp. 211–214. EDP Sciences, April 22-27, 2007, Nice, France (2008)
45. L. McFadden, G.R. Satchler, Optical-model analysis of the scattering of 24.7 Mev alpha particles. Nucl. Phys. **84**(1), 177–200 (1966). https://doi.org/10.1016/0029-5582(66)90441-X
46. P. Demetriou, C. Grama, S. Goriely, Improved global α-optical model potentials at low energies. Nucl. Phys. A **707**(1), 253–276 (2002). https://doi.org/10.1016/S0375-9474(02)00756-X
47. V. Avrigeanu, M. Avrigeanu, C. Mănăilescu, Further explorations of the α-particle optical model potential at low energies for the mass range $A \approx$45-209. Phys. Rev. C **90**, 044612 (2014). https://doi.org/10.1103/PhysRevC.90.044612
48. P. Mohr, Z. Fülöp, G. Gyürky, G.G. Kiss, T. Szücs, Successful prediction of total α-induced reaction cross sections at astrophysically relevant sub-Coulomb energies using a novel approach. Phys. Rev. Lett. **124**, 252701 (2020). https://doi.org/10.1103/PhysRevLett.124.252701
49. P. Mohr, Z. Fülöp, G. Gyürky, G.G. Kiss, T. Szücs, A. Arcones, M. Jacobi, A. Psaltis, Astrophysical reaction rates of α-induced reactions for nuclei with $26 \leq Z \leq 83$ from the new Atomki-V2 α-nucleus potential. At. Data Nucl. Data Tables **142**, 101453 (2021). https://doi.org/10.1016/j.adt.2021.101453
50. S. Watanabe, High energy scattering of deuterons by complex nuclei. Nucl. Phys. **8**, 484–492 (1958). https://doi.org/10.1016/0029-5582(58)90180-9
51. M. Nolte, H. Machner, J. Bojowald, Global optical potential for α particles with energies above 80 Mev. Phys. Rev. C **36**, 1312–1316 (1987). https://doi.org/10.1103/PhysRevC.36.1312
52. V. Avrigeanu, P.E. Hodgson, M. Avrigeanu, Global optical potentials for emitted alpha particles. Phys. Rev. C **49**, 2136–2141 (1994). https://doi.org/10.1103/PhysRevC.49.2136
53. T. Rauscher, Relevant energy ranges for astrophysical reaction rates. Phys. Rev. C **81**, 045807 (2010). https://doi.org/10.1103/PhysRevC.81.045807
54. P. Mohr, α-induced reaction cross sections in the mass range $A \approx 20-50$: a critical review. J. Phys: Conf. Ser. **940**, 012015 (2018). https://doi.org/10.1088/1742-6596/940/1/012015
55. T. Rauscher, computer code NON- SMOKER(WEB) (2001). http://nucastro.org/websmoker.html/
56. R.H. Cyburt, A.M. Amthor, R. Ferguson, Z. Meisel, K. Smith, S. Warren, A. Heger, R.D. Hoffman, T. Rauscher, A. Sakharuk, H. Schatz, F.K. Thielemann, M. Wiescher, The jina reaclib database: Its recent updates and impact on type-I X-ray bursts. Astrophys. J. Suppl. Ser. **189**(1), 240 (2010)
57. E. Somorjai, Z. Fülöp, A.Z. Kiss, C.E. Rolfs, H.P. Trautvetter, U. Greife, M. Junker, S. Goriely, M. Arnould, M. Rayet, T. Rauscher, H. Oberhummer, Experimental cross section of ^{144}Sm$(\alpha,\gamma)^{148}$Gd and implications for the p-process. Astronomy & Astrophysics **333**, 1112–1116 (1998)
58. N.N. Le, N.Q. Hung, Improved version of the α-nucleus optical model potential for reactions relevant to the γ process. Phys. Rev. C **105**, 014602 (2022). https://doi.org/10.1103/PhysRevC.105.014602
59. D. Basak, C. Basu, Determination of α-optical potential for reactions with p-nuclei from the study of (α, n) reactions in the astrophysically relevant energy region. The European Physical Journal A **58**(8), 150 (2022). https://doi.org/10.1140/epja/s10050-022-00798-4
60. T. Szücs, G.G. Kiss, G. Gyürky, Z. Halász, Z. Fülöp, T. Rauscher, Cross section of α-induced reactions on iridium isotopes obtained from thick target yield measurement for the astrophysical γ process. Phys. Lett. B **776**, 396–401 (2018). https://doi.org/10.1016/j.physletb.2017.11.072
61. G.G. Kiss, T. Szücs, T. Rauscher, Z. Török, Z. Fülöp, G. Gyürky, Z. Halász, E. Somorjai, Alpha induced reaction cross section measurements on ^{162}Er for the astrophysical γ process. Phys. Lett. B **735**, 40–44 (2014). https://doi.org/10.1016/j.physletb.2014.06.011
62. A. Sauerwein, H.-W. Becker, H. Dombrowski, M. Elvers, J. Endres, U. Giesen, J. Hasper, A. Hennig, L. Netterdon, T. Rauscher, D. Rogalla, K.O. Zell, A. Zilges, Determination of ^{141}Pr$(\alpha, n)^{144}$Pm cross sections at energies of relevance for the astrophysical p process using the $\gamma\gamma$ coincidence method. Phys. Rev. C **84**, 045808 (2011). https://doi.org/10.1103/PhysRevC.84.045808
63. T. Rauscher, G.G. Kiss, T. Szücs, Z. Fülöp, C. Fröhlich, G. Gyürky, Z. Halász, Z. Kertész, E. Somorjai, Astrophysical analysis of the measurement of (α,γ) and (α,n) cross sections of ^{169}Tm. Phys. Rev. C **86**, 015804 (2012). https://doi.org/10.1103/PhysRevC.86.015804
64. L. Netterdon, P. Demetriou, J. Endres, U. Giesen, G.G. Kiss, A. Sauerwein, T. Szücs, K.O. Zell, A. Zilges, Investigation of α-induced reactions on the p nucleus Yb-168. Nucl. Phys. A **916**, 149–167 (2013). https://doi.org/10.1016/j.nuclphysa.2013.08.002
65. J. Glorius, K. Sonnabend, J. Görres, D. Robertson, M. Knörzer, A. Kontos, T. Rauscher, R. Reifarth, A. Sauerwein, E. Stech, W. Tan, T. Thomas, M. Wiescher, Experimental cross sections of ^{165}Ho$(\alpha, n)^{168}$Tm and ^{166}Er$(\alpha, n)^{169}$Yb for optical potential studies relevant for the astrophysical γ process. Phys. Rev. C **89**, 065808 (2014). https://doi.org/10.1103/PhysRevC.89.065808
66. M. Avrigeanu, V. Avrigeanu, α-particle nuclear surface absorption below the Coulomb barrier in heavy nuclei. Phys. Rev. C **82**, 014606 (2010). https://doi.org/10.1103/PhysRevC.82.014606

67. T. Szücs, P. Mohr, G. Gyürky, Z. Halász, R. Huszánk, G.G. Kiss, T.N. Szegedi, Z. Török, Z. Fülöp, Activation measurement of α-induced cross sections for ^{197}Au: analysis in the statistical model and beyond. J. Phys: Conf. Ser. **1668**(1), 012042 (2020). https://doi.org/10.1088/1742-6596/1668/1/012042
68. G.R. Satchler, W.G. Love, Folding model potentials from realistic interactions for heavy-ion scattering. Phys. Rep. **55**(3), 183–254 (1979). https://doi.org/10.1016/0370-1573(79)90081-4
69. A.M. Kobos, B.A. Brown, R. Lindsay, G.R. Satchler, Folding-model analysis of elastic and inelastic α-particle scattering using a density-dependent force. Nucl. Phys. A **425**(2), 205–232 (1984). https://doi.org/10.1016/0375-9474(84)90073-3
70. P. Mohr, α-nucleus potentials for the neutron-deficient p nuclei. Phys. Rev. C **61**, 045802 (2000). https://doi.org/10.1103/PhysRevC.61.045802
71. P. Scholz, H. Wilsenach, H.W. Becker, A. Blazhev, F. Heim, V. Foteinou, U. Giesen, C. Münker, D. Rogalla, P. Sprung, A. Zilges, K. Zuber, New measurement of the ^{144}Sm$(\alpha,\gamma)^{148}$Gd reaction rate for the γ process. Phys. Rev. C **102**, 045811 (2020). https://doi.org/10.1103/PhysRevC.102.045811
72. Z. Mátyus, G. Gyürky, P. Mohr, A. Angyal, Z. Halász, G.G. Kiss, A. Tóth, T. Szücs, Z. Fülöp, Low-energy α-nucleus optical potential studied via (α, n) cross section measurements on Te isotopes. Phys. Rev. C **109**, 065806 (2024). https://doi.org/10.1103/PhysRevC.109.065806
73. M. Avrigeanu, W. von Oertzen, A. Plompen, V. Avrigeanu, Optical model potentials for α-particles scattering around the Coulomb barrier on $A \sim 100$ nuclei. Nucl. Phys. A **723**(1), 104–126 (2003). https://doi.org/10.1016/S0375-9474(03)01159-X
74. M. Avrigeanu, W. von Oertzen, V. Avrigeanu, On temperature dependence of the optical potential for alpha-particles at low energies. Nucl. Phys. A **764**, 246–260 (2006). https://doi.org/10.1016/j.nuclphysa.2005.10.001
75. V. Avrigeanu, M. Avrigeanu, Validation of an optical potential for incident and emitted low-energy α-particles in the $A \sim 60$ mass range. The European Physical Journal A **57**(2), 54 (2021). https://doi.org/10.1140/epja/s10050-020-00336-0
76. V. Avrigeanu, M. Avrigeanu, Validation of an optical potential for incident and emitted low-energy α-particles in the $A \sim 60$ mass range. The European Physical Journal A **58**(9), 189 (2022). https://doi.org/10.1140/epja/s10050-022-00831-6
77. M. Avrigeanu, V. Avrigeanu, Consistent optical potential for incident and emitted low-energy α particles. iii. nonstatistical processes induced by neutrons on Zr, Nb, and Mo nuclei. Phys. Rev. C **107**, 034613 (2023). https://doi.org/10.1103/PhysRevC.107.034613
78. A. Palumbo, W.P. Tan, J. Görres, M. Wiescher, N. Özkan, R.T. Güray, C. Yalcin, Measurement of ^{120}Te(α,n) cross sections relevant to the astrophysical p process. Phys. Rev. C **85**, 028801 (2012). https://doi.org/10.1103/PhysRevC.85.028801
79. B.B. Back, H. Esbensen, C.L. Jiang, K.E. Rehm, Recent developments in heavy-ion fusion reactions. Rev. Mod. Phys. **86**, 317–360 (2014). https://doi.org/10.1103/RevModPhys.86.317
80. K. Hagino, N. Takigawa, Subbarrier Fusion Reactions and Many-Particle Quantum Tunneling. Progress of Theoretical Physics **128**(6), 1061–1106 (2012) https://doi.org/10.1143/PTP.128.1061http://oup.prod.sis.lan/ptp/article-pdf/128/6/1061/9681414/128-6-1061.pdf
81. A.B. Balantekin, N. Takigawa, Quantum tunneling in nuclear fusion. Rev. Mod. Phys. **70**, 77–100 (1998). https://doi.org/10.1103/RevModPhys.70.77
82. L.F. Canto, R. Donangelo, M.S. Hussein, P. Lotti, J. Lubian, J. Rangel, Theoretical considerations about heavy-ion fusion in potential scattering. Phys. Rev. C **98**, 044617 (2018). https://doi.org/10.1103/PhysRevC.98.044617
83. V. Zagatto, C.E. Aguiar, J. Lubian, L.F. Canto, Compound nucleus formation effects in heavy-ion fusion cross sections. Phys. Rev. C **111**, 024617 (2025). https://doi.org/10.1103/PhysRevC.111.024617
84. C. Fougères, M.L. Avila, H. Jayatissa, D. Santiago-Gonzalez, K. Brandenburg, Z. Meisel, P. Mohr, F. Montes, C. Müller-Gatermann, D. Neto, W.-J. Ong, J. Pereira, K.E. Rehm, T.L. Tang, I.A. Tolstukhin, L. Varriano, G. Wilson, J. Wu, Direct cross-section measurement of the weak r-process ^{88}Sr$(\alpha, n)^{91}$Zr reaction in ν-driven winds of core-collapse supernovae. Phys. Rev. C **109**, 065805 (2024). https://doi.org/10.1103/PhysRevC.109.065805
85. L.C. Chamon, B.V. Carlson, L.R. Gasques, D. Pereira, C. De Conti, M. Alvarez, M.S. Hussein, M.A. Cândido Ribeiro, E.S. Rossi, C.P. Silva, Toward a global description of the nucleus-nucleus interaction. Phys. Rev. C **66**, 014610 (2002). https://doi.org/10.1103/PhysRevC.66.014610
86. L.R. Gasques, Celebrating 20 Years of the São Paulo Potential. Braz. J. Phys. **51**, 269–276 (2021)
87. L.C. Chamon, B.V. Carlson, L.R. Gasques, São paulo potential version 2 (spp2) and brazilian nuclear potential (bnp). Comput. Phys. Commun. **267**, 108061 (2021). https://doi.org/10.1016/j.cpc.2021.108061
88. H. Guo, Y. Xu, H. Liang, Y. Han, Q. Shen, ^{4}He microscopic optical model potential. Phys. Rev. C **83**, 064618 (2011). https://doi.org/10.1103/PhysRevC.83.064618
89. V. Durant, P. Capel, α-nucleus optical potentials from chiral effective field theory nn interactions. Phys. Rev. C **105**, 014606 (2022). https://doi.org/10.1103/PhysRevC.105.014606
90. V.Y. Denisov, Alpha-decay half-lives and alpha-capture cross-sections. At. Data Nucl. Data Tables **161**, 101684 (2025). https://doi.org/10.1016/j.adt.2024.101684
91. V.Y. Denisov, A.A. Khudenko, α-decay half-lives, α-capture, and α-nucleus potential. At. Data Nucl. Data Tables **95**(6), 815–835 (2009). https://doi.org/10.1016/j.adt.2009.06.003
92. V.Y. Denisov, O.I. Davidovskaya, I.Y. Sedykh, Improved parametrization of the unified model for α decay and α capture. Phys. Rev. C **92**, 014602 (2015). https://doi.org/10.1103/PhysRevC.92.014602
93. P. Mohr, α-decay half-life of ^{212}Po at stellar temperatures. J. Phys. G: Nucl. Part. Phys. **50**(7), 075103 (2023). https://doi.org/10.1088/1361-6471/acd39a
94. P. Mohr, α-decay properties of ^{296}118 from double-folding potentials. Phys. Rev. C **95**, 011302 (2017). https://doi.org/10.1103/PhysRevC.95.011302
95. P. Mohr, α-nucleus potentials, α-decay half-lives, and shell closures for superheavy nuclei. Phys. Rev. C **73**, 031301 (2006). https://doi.org/10.1103/PhysRevC.73.031301
96. H.P. Graf, H. Münzel, Excitation functions for α-particle reactions with molybdenum isotopes. J. Inorg. Nucl. Chem. **36**(12), 3647–3657 (1974). https://doi.org/10.1016/0022-1902(74)80143-0
97. R.A. Esterlund, B.D. Pate, Analysis of excitation functions via the compound statistical model: Angular momentum effects. Nucl. Phys. **69**(2), 401–422 (1965). https://doi.org/10.1016/0029-5582(65)90059-3
98. A.L. Sallaska, C. Iliadis, A.E. Champagne, S. Goriely, S. Starrfield, F.X. Timmes, Starlib: A next-generation reaction-rate library for nuclear astrophysics. Astrophys. J. Suppl. Ser. **207**(1), 18 (2013)
99. G.G. Kiss, S.R. Kovács, T.N. Szegedi, P. Mohr, F. Montes, A. Arcones, A. Tóth, A. Németh, E. Szilágyi, M. Kumar Pal, M. Braun, Z. Halász, Z. Elekes, G. Gyürky, T. Szücs, Low energy measurement of the ^{86}Kr$(\alpha$,n$)^{89}$Sr reaction cross section and its impact on weak r-process nucleosynthesis. Astroph. J., submitted (2025)

100. C. Fougères, M.L. Avila, A. Psaltis, A. Anastasiou, S. Bae, L. Balliet, K. Bhatt, L. Dienis, H. Jayatissa, V. Karayonchev, P. Mohr, F. Montes, D. Neto, F. de Oliveira Santos, W.-J. Ong, K.E. Rehm, W. Reviol, D. Santiago-Gonzalez, N. Sensharma, R.S. Sidhu, I.A. Tolstukhin, First measurement of ^{87}Rb(α,xn) cross sections at weak r-process energy in supernova ν-driven ejecta to investigate elemental abundances in low-metallicity stars. Astroph. J. **983**(2), 142 (2025). https://doi.org/10.3847/1538-4357/adc253
101. G.G. Kiss, T.N. Szegedi, P. Mohr, M. Jacobi, G. Gyürky, R. Huszánk, A. Arcones, Low-energy measurement of the ^{96}Zr(α, n)^{99}Mo reaction cross section and its impact on weak r-process nucleosynthesis. Astrophys. J. **908**(2), 202 (2021). https://doi.org/10.3847/1538-4357/abd2bc
102. G. Gyürky, P. Mohr, A. Angyal, Z. Halász, G.G. Kiss, Z. Mátyus, T.N. Szegedi, T. Szücs, Z. Fülöp, Cross section measurement of the ^{144}Sm(α, n)^{147}Gd reaction for studying the α-nucleus optical potential at astrophysical energies. Phys. Rev. C **107**, 025803 (2023). https://doi.org/10.1103/PhysRevC.107.025803
103. A. Psaltis, A. Arcones, F. Montes, P. Mohr, C.J. Hansen, M. Jacobi, H. Schatz, Constraining nucleosynthesis in neutrino-driven winds: Observations, simulations, and nuclear physics. Astrophys. J. **935**(1), 27 (2022). https://doi.org/10.3847/1538-4357/ac7da7
104. R. Kumar, S. Rana, M. Bhuyan, P. Mohr, Fusion cross section of α-induced reactions for heavy target nuclei. Phys. Rev. C **105**, 044606 (2022). https://doi.org/10.1103/PhysRevC.105.044606